Contents lists available at SciVerse ScienceDirect

CIRP Annals Manufacturing Technology

Journal homepage: www.elsevier.com/locate/cirp

Advances in the metrological traceability and performance of X-ray computed tomography

Wim Dewulf (1)[a], Harald Bosse (3)[b], Simone Carmignato (1)[c], Richard Leach (1)[d]

[a] *KU Leuven, Belgium*
[b] *Physikalisch-Technische Bundesanstalt (PTB), Germany*
[c] *University of Padova, Italy*
[d] *University of Nottingham, United Kingdom*

X-ray computed tomography (XCT) is increasingly being used for evaluating quality and conformance of complex products, including assemblies and additively manufactured parts. The metrological performance and traceability of XCT nevertheless remains an important research area that is reviewed in this paper. The error sources influencing XCT measurement results are discussed, along with related qualification, calibration and optimization procedures. Moreover, progress on performance verification testing and on the determination of task-specific measurement uncertainty is covered. Results of interlaboratory comparisons are summarized and performance in various dimensional measurement fields is illustrated. Conclusions and an outlook for future research activities are also provided.

X-ray, Metrology, Traceability

1. Introduction

Companies in various sectors (automotive, aerospace, energy, medical,...) are increasingly relying on X-ray computed tomography to evaluate quality and conformance of complex parts. This introduction briefly describes the principle of X-ray computed tomography, as a basis for a more elaborate discussion on metrological traceability and performance in subsequent sections.

1.1. X-ray computed tomography

X-ray computed tomography (X-ray CT or XCT) is defined as an imaging method using X-ray attenuation through material of an object and computer algorithms to reconstruct two-dimensional (2D) images of an object, representing cross-sectional slices through the object, or three-dimensional (3D) representations of the object's structure, including inner geometries [69]. After successful applications in the medical field since the 1970s, and for material analysis and non-destructive testing since the 1980s, XCT has exhibited substantial growth in more quantitative industrial applications such as dimensional quality control since 2005 ([63],[95],[166]).

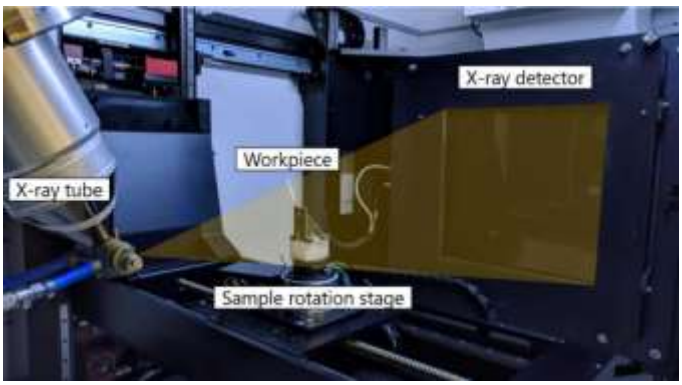

Fig. 1. Main components of an industrial XCT device [94].

The use of XCT for industrial quality control is typically based on so called cabinet XCT systems, which employ X-ray tube sources and rely on the principle of X-ray attenuation contrast. Details on other X-ray sources (including synchrotron sources and linear accelerators) and different imaging modalities (including phase contrast XCT) are given elsewhere [293]. The most common architecture of an industrial XCT device is depicted in Fig. 1. X-rays are generated inside an X-ray source that relies on the principle of a hot cathode tube (Fig. 2). A cathode – usually a tungsten filament – generates free electrons due to the thermionic effect caused by the flow of electric current. Under influence of an applied potential difference, these electrons are accelerated towards a target on the tube anode. A set of electronic lenses focuses the beam of accelerated electrons onto a focal spot on the anode target. Upon incidence on the target, approximately 1% of the electron energy is converted into X-ray photons, while the remaining energy is converted into heat. Hence, active cooling of the source anode is critical to ensure dissipation of this heat.

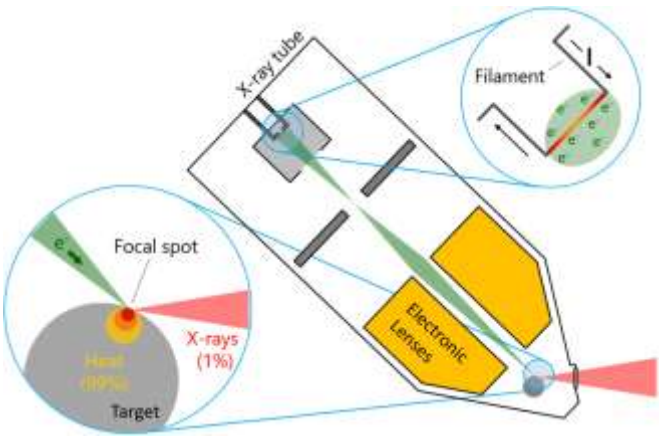

Fig. 2. Schematic representation of a typical hot cathode X-ray tube with a reflection target (based on [94]).

The emitted X-rays penetrate the workpiece that is mounted on a rotation stage, at which point they are attenuated due to a combination of material- and energy-dependent interactions, including the photoelectric absorption, Compton scattering, Rayleigh/Thomson scattering and (at voltages > 1MeV) pair production. The attenuation of X-rays follows the Beer-Lambert law:

$$I(L) = \int_0^{E_{max}} I_0(E) e^{-\int_0^L \mu(E,x)dx}\, dE \qquad (1)$$

where $I(L)$ represents the attenuated X-ray intensity after penetrating a path length L, E is the photon energy, and $\mu(E,x)$ is the energy-specific attenuation coefficient at position x along the path of the X-rays. The intensity of the attenuated X-rays is quantified with a suitable detector, yielding a projection; also referred to as radiograph in the medical field. The rotation stage allows projections to be obtained from different angular perspectives of the workpiece, which can subsequently be used to reconstruct a 3D volumetric attenuation model (for flat panel detectors) or 2D cross-section (for linear detectors) using a mathematical reconstruction algorithm derived from the inverse Radon transform. Each voxel of this 3D model, or pixel of the 2D cross-section, is assigned a grey value that is representative of the X-ray attenuation incurred within the volumetric extent of the voxel [95]. More elaborate descriptions on the X-ray physics and reconstruction algorithms can be found elsewhere ([54],[63],[68],[154],[190],[238]). After subsequent surface determination (segmentation), dimensional measurements can be performed. The full workflow is illustrated in Fig. 3.

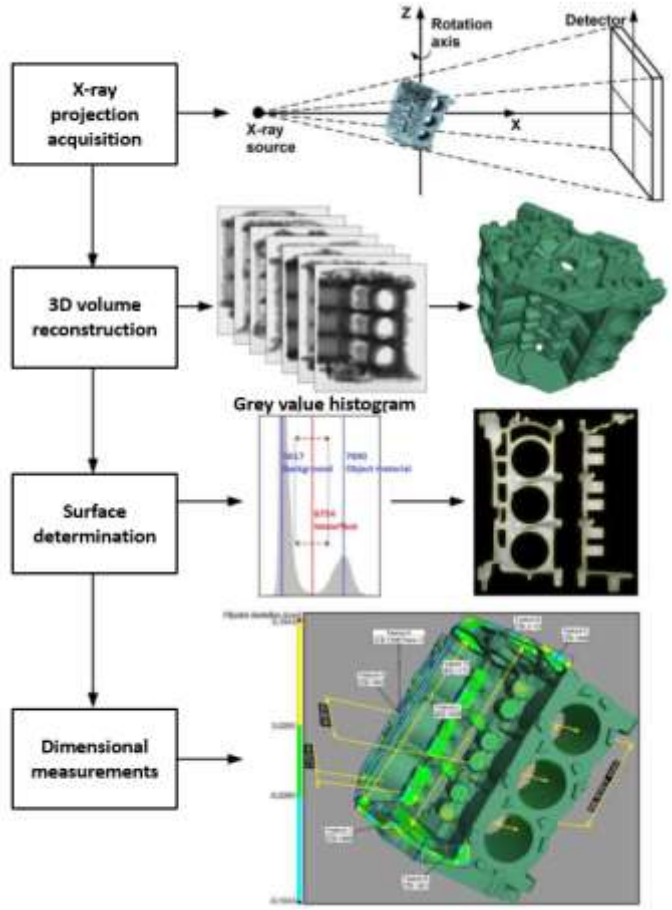

Fig. 3. XCT Workflow (based on [276]).

A key advantage of XCT for dimensional measurements over tactile or optical systems is its ability to measure the complete inner and outer geometry of a workpiece in one single acquisition, while enabling simultaneous material defect detection with data acquisition times that are relatively independent of part geometric complexity (Fig. 4). Limitations of XCT include its dependence on numerous influence quantities (Fig. 5), which can result in significant issues with measurement traceability and size limitations in terms of maximum material penetration (Tab. 1).

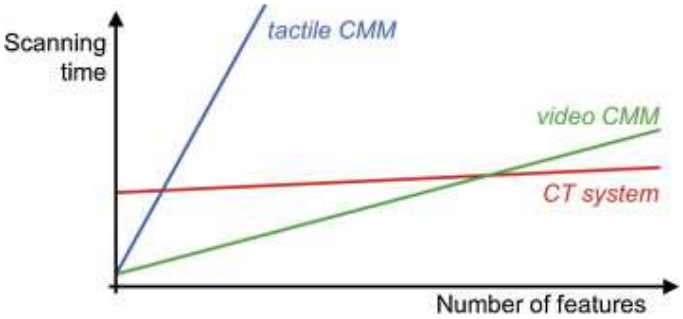

Fig. 4. Scanning time as a function of part complexity [73].

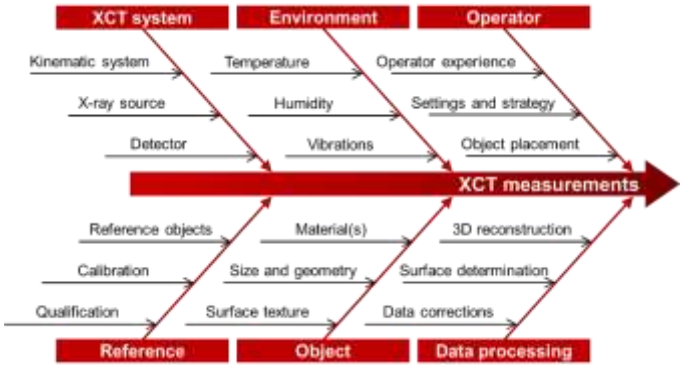

Fig. 5. Ishikawa diagram for XCT influence factors.

Table 1
Examples of material penetration limitations [67].

X-ray voltage	*130 kV*	*150 kV*	*190 kV*	*225 kV*	*450 kV*
Steel/ceramic	5 mm	<8 mm	<25 mm	<40 mm	<70 mm
Aluminium	<30 mm	<50 mm	<90 mm	<150 mm	<250 mm
Plastic	<90 mm	<130 mm	<200 mm	<250 mm	<450 mm

1.2. Outline and scope

Extensive reviews of the potential of XCT for dimensional measurements [166] and of its industrial applications [73] are provided elsewhere. This keynote will focus on recent advances in the metrological performance and traceability of XCT. Sections 2 to 4 will provide an overview of the error sources influencing XCT measurement results. A distinction is made between influence factors related to the XCT device and environment (Section 2); operator decisions (Section 3); and the data processing pipeline (Section 4). Influence factors as well as qualification, calibration and optimization procedures are discussed. Subsequently, Section 5 provides an overview of performance verification tests. Different methods for determining task-specific measurement uncertainty

form the subject of Section 6, which precedes an overview of interlaboratory comparisons in Section 7. The latter section provides an overview of performance in various dimensional measurement applications, including geometry measurements, surface measurements, porosity measurements, and composite materials measurements. Conclusions and an outlook for future research activities are provided in Section 8.

2. XCT device and environment related influence factors

This section covers XCT device and environmental error sources. While the evaluation of task-specific measurement uncertainty is discussed in Section 6, this section focuses on the characterization of error sources independently of the final measurement task. Such characterizations are requirements for system calibration. In addition, to optimize the performance of the XCT system and its components and to achieve the specifications of the manufacturer, the experiments conducted for testing specific error conditions can be followed by the determination of parameters used for adjustments of the system. These experiments and adjustments are known as XCT system qualification [29]. Elements to be characterized and qualified concern the kinematic system (namely the relative positions and orientations of source, detector, linear axes and rotary axis) and the X-ray source focal spot characteristics (position, size, shape and spectral information), as well as the distortion and intensity response of the detector.

2.1 Kinematic system

In an ideal kinematic system, the main axes are determined based on the rotation axis of the sample stage and the magnification axis, which is defined by the line from the X-ray focal spot that intersects the rotation axis orthogonally (Fig. 6). The detector is ideally centred and aligned orthogonally to the magnification axis and parallel to the rotation axis[90]. The reconstruction algorithms assume that the kinematic system geometry is ideal or that all positions and orientations of the system's components are accurately known. Discrepancies between the assumed and the actual geometry will lead to deviations in the reconstructed model.

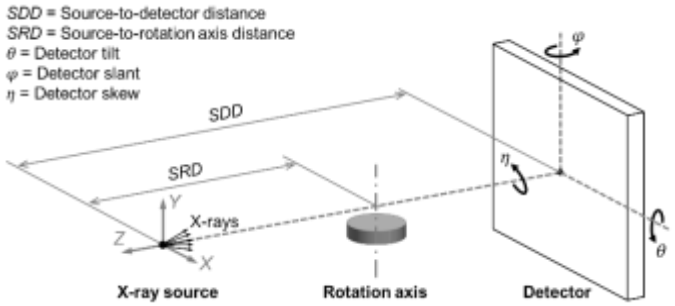

Fig. 6. Schematic representation of the kinematic system of a cone-beam XCT system (adapted from [229]).

The influence of positional and angular deviations within the kinematic system has been widely investigated and is summarized in Table 2. Most studies rely on multi-sphere artefacts [64] that enable separation of local form deviations, associated with blurred edges and image artifacts, and deviations of long, unidirectional distances ([5],[91],[167],[194]) (Fig. 7). Position errors along the Z-axis (magnification axis) yield uniform voxel size errors, implying an unknown scaling of the workpiece model without inducing form errors. In contrast, position errors along the X- and Y-axes may yield local form deviations in the reconstruction, but without significantly influencing unidirectional dimensions throughout the volume. Angular misalignments of the detector relative to the source-rotation stage assembly concern tilt, slant and skew (θ, φ and η respectively in Fig. 6). In the presence of a detector tilt, the magnification factor varies along the vertical direction of the reconstructed model, yielding dimensional errors. Nevertheless, perceptual image quality is little affected, since within each reconstructed slice magnification factor variations are negligible. The presence of detector slant or skew, however, induces important blurring of the edges due to inconsistent projection data. Image quality has been shown to be especially sensitive to uncorrected detector skew, yielding pronounced form deviations in reconstructed spheres.

The length scale of XCT reconstructed volumes is provided by the voxel size, whose determination is, therefore, fundamental for establishing the metrological traceability of XCT dimensional measurements. In general, the voxel size is given by the detector pixel size divided by the magnification factor, which is the ratio of the source-to-detector distance (SDD) and the source-to-rotation axis distance (SRD) (See Fig. 6). For aligned XCT systems, the voxel size can then be calibrated by determining the SDD and the SRD prior to reconstruction or by applying different methods [95]. E.g., Illemann et al. [132] use a printed circuit board (PCB) with a calibrated grid of circular holes to determine the actual magnification factor from the ratio of the projected and the calibrated hole positions. The same PCB was used to establish the alignment of the rotation axis with respect to the detector, from the analysis of the trapezoidal distortions of the projected hole grid. Two X-ray projections of the PCB, acquired at 180° angular displacements of the rotary stage, allow separation of the tilts and offsets of the rotation axis from those of the PCB. In a later paper Illemann et. al. used a thin foil made of invar containing an etched hole grid instead of the PCB [134].

When the detector is aligned orthogonally to the magnification axis and the magnification axis intersects the detector in its geometrical centre, the SDD and the SRD can be individually determined (in addition to their ratio) from the X-ray projections of a calibrated artefact acquired at multiple positions of either stage or detector ([95],[134]). Illemann et al. [134] allowed accurate determination of the focal spot and detector positions; showing their dependency on the X-ray spectrum and hence on the specific scanning parameters (see Section 3.1), and demonstrating the importance of accurate alignment of the critical tube components to reduce the variations of the focal spot position at different tube voltages. In the case of high-resolution XCT systems with a small field of view, Zemek et al. [312] proposed the use of a small artefact, with calibrated centre-to-centre sphere distance below 1 mm, for determining the SDD and SRD from the projections of the artefact acquired at multiple SDDs.

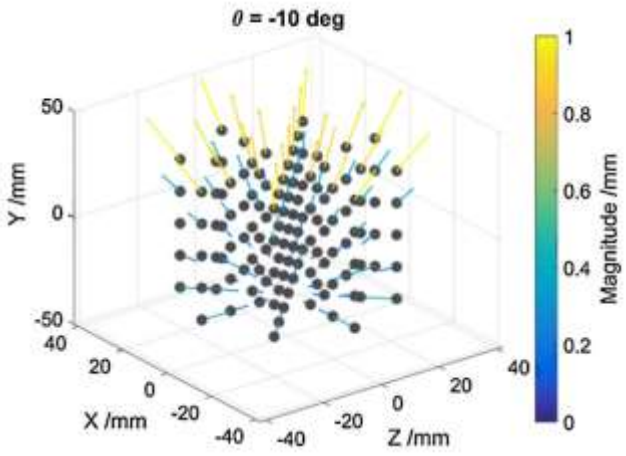

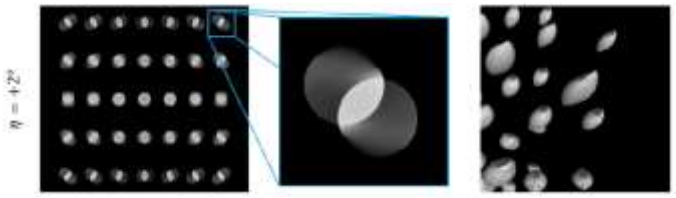

Fig. 7. Influence of detector misalignments on volumetric unidirectional distances and on form [91].

Table 2
Influence of positional and angular deviations on unidirectional distances and on form deviations. Based on ([5],[91],[96],[167],[194],[229]).

Error type	*Influence on long (unidirectional) distances*	*Influence on image quality and local form deviations*
Position error along X	Limited	Yes
Position error along Y	Limited	Yes
Position error along Z	Significant with constant scale factor in all three dimensions	No
Angular error along X	Primarily within horizontal planes far from the central slice	Limited
Angular error along Y	Primarily within horizontal planes; limited influence on vertical distances	Yes
Angular error along Z	Limited	Significant
Source drift	Limited	Limited
Rotation stage error motion	Limited	Yes

The length scale can be calibrated also post-reconstruction, from XCT measurements of calibrated lengths in the scanned volume, followed by voxel rescaling. E.g., Stolfi and De Chiffre [254] propose a tubular calibrated artefact to be scanned together with the workpiece, hence compressing the time required into a single scan process. Other authors, such as Katić et al. [156], proposed alternative solutions, where the calibrated lengths are embedded directly in the workpiece itself. These approaches using post-reconstruction corrections of the voxel size are subject to potential errors due to a rescaling process that is based on data reconstructed from an uncorrected back-projection geometry [76].

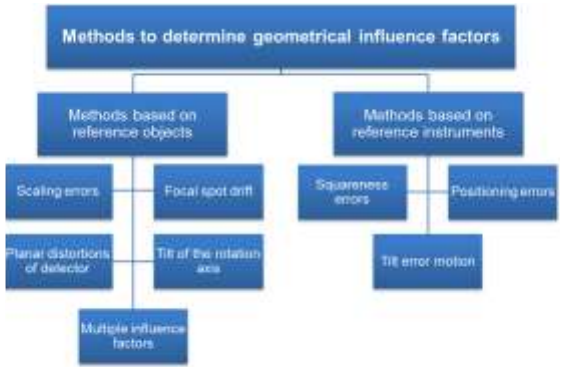

Fig. 8. Classification of methods used for determining the geometry of XCT systems [90].

When the detector is not aligned with respect to the rotation stage, a pre-reconstruction procedure is essential to evaluate the full system geometry needed for accurate scale calibration (Fig. 8). To determine the geometrical errors, reference instruments including interferometers and electronic levels can be used. The Swiss Federal Institute of Metrology (METAS) developed an XCT system comprising eight fibre interferometers and five straightness sensors for XCT traceability research [38]. Alternatively, the geometrical parameters of the XCT system can be calibrated by minimization of reprojection errors performed from a set of X-ray projections of a calibrated artefact [92]. Then the determined misalignments can be corrected either through physical adjustment of the system geometry [93] or through reconstruction algorithms that consider the misaligned geometry in the back-projection [8]. Multiple calibrated artefacts of different sizes may be required to achieve high sensitivity to motion errors of the sample stage at all magnification positions [96]. A parametrisation using seven degrees of freedom (DoF) is sufficient when assuming a static XCT system geometry [9]; however, when considering a dynamic system geometry, e.g. due to thermal effects and drift, a larger number of DoF is required [39].

2.2 X-ray source and focal spot

The X-ray source has a major impact on the quality of the projections, and hence on that of the XCT reconstruction and on dimensional measurements. In Section 3.1, the influences of settings directly controlled by the user are discussed, including target material, acceleration voltage, current, and hardware filter; all affecting the X-ray spectrum produced. The discussion in this section will, therefore, be delineated by aspects only indirectly influenced by the user, i.e. the electron beam alignment, focal spot size, shape and position.

In the last decades, X-ray sources have undergone considerable progress and research activities have significantly improved the performances achievable with X-ray tubes. For example, nano-focus sources enable the investigation of details too small to be discerned by micro-focus XCT [293], whereas liquid metal sources [173], compact light sources [126], microstructured targets [305] and laser-driven sources [109] allow to increase the attainable flux, hence reducing the difference between tube and synchrotron sources [252]. The following discussion will concentrate on the most common type of X-ray source used in industrial XCT – the X-ray tube with filament cathode and solid anode (see Fig. 2).

In a typical X-ray tube, the filament, which emits electrons due to the thermionic effect, consists of a tungsten wire bent into a V-shaped knuckle and placed inside a Wehnelt cylinder, which serves as an electrostatic lens concentrating the emission of electrons at the tip of the knuckle. Therefore, correct positioning and centering of the so called 'hairpin' filament within the Wehnelt cylinder during its replacement is essential [290]. For example, Townsend et al. [268] reported a 1 % change in surface areal parameters of a measured sample after filament change. Electronic lenses further steer and focus the accelerated electrons towards the target. When changing the source settings, the electron beam needs to be realigned to avoid focal spot shift and associated scatter inside the X-ray tube, which degrades the signal-to-noise ratio ([101],[215]).

A non-ideal focal spot (i.e. with a finite size and possibly a non-symmetrical shape) yields blurring of the projections, which consequently affects the reconstructed 3D models in terms of reduced edge sharpness and structural resolution. Specification standards, such as EN 12543-5 [86], ASTM E1165 [17], and IEC 60336 [129], describe the procedures for qualifying the focal spot width and height. These procedures rely on a small, detailed structures placed in front of the X-ray source and imaged with the highest possible magnification; examples of such structures are the QRM Micro CT Bar Pattern NANO Phantom, the JIMA mask and the Siemens star [29]. Probst et al. [217] applied the inverse Radon transform to a series of line spread functions (LSFs) obtained from a projection of the Siemens star pattern to reconstruct a 2D intensity profile of the focal spot (see Fig. 9). Similar approaches have been proposed based on a disk [77] or a rotating edge [241]. Baier et al. [18] furthermore implemented a star-pattern-based method for automated evaluation of the modulation transfer function (MTF) and focal spot characteristics (Fig. 10).

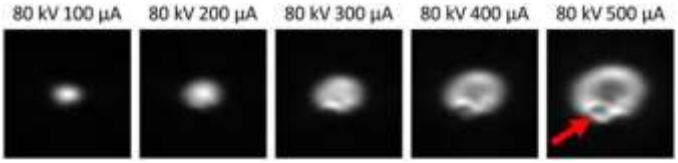

Fig. 9. 2D images of the focal spot reconstructed through the inverse Radon transform on projections of a Siemens star pattern at different settings; the red arrow indicates a localized intensity variation attributed to the pitting of the target material [217].

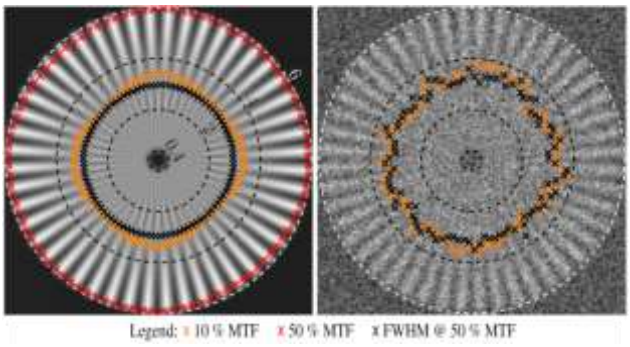

Fig. 10. Focal spot characterization performed using a star pattern [19]. Left: spatial resolution limits (radial scale in micrometres) determined on a simulated X-ray projection without noise contribution. Right: same as the image on the left but for the flat-field corrected projection with all system components contributing to the resolution.

The shape and position of the focal spot may change during use, e.g. depending on the X-ray source settings (i.e. voltage and current, and hence power), which are typically varied substantially based on the application (Fig. 9). Higher powers demand larger spot sizes to avoid target damage due to the increased heat load on the target. Electron optics control the focal spot size and position, with diameter dilation of 1 µm·W^{-1} being common [199]. The orientation of the target with respect to both the incident electron beam and the X-ray window of the source assembly moreover determine the effective size of the focal spot, though this design parameter is limited by the occurrence of electron backscatter. The temperature variation may change the focal spot position, hence influencing distances between the different components of the XCT device. Also, filament changes result in position changes of the focal spot. The influence is largest when scanning at high magnification, e.g. with the aim of areal surface texture data extraction [268]. Therefore, performing several new qualifications (e.g. of the voxel size) is necessary during the use of a XCT system.

During acquisition, the X-ray tube is subject to thermal expansion due to the heat load, which results in the focal spot drift ([122],[283]). Although the focal spot positional instabilities are mainly due to thermal effects, they can also be due to, e.g., unstable magnetic focusing inside the X-ray source that produces spatial fluctuations of the accelerated electron beam. Typically, external cooling can significantly reduce this drift, but does not completely eliminate it [216]. Fig. 11 shows the results of measurements of the focus drift performed immediately after the warm-up phase of an X-ray tube [122].

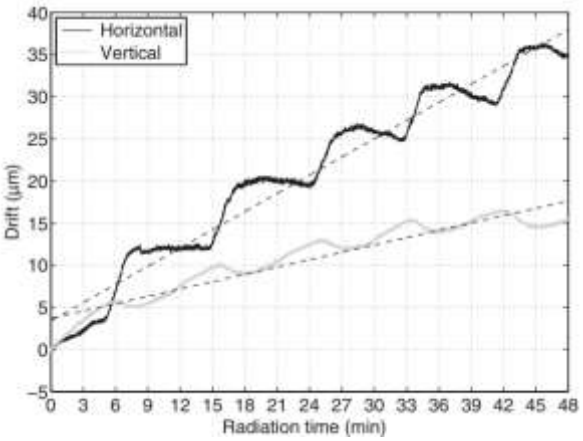

Fig. 11. Example of focal spot drift in the horizontal (X) and vertical (Y) spatial directions, after an effective warm-up time of approximately 20 minutes. The dashed lines are least-squares fitted curves that can be subsequently used to compensate the drift [122].

Different methods can be applied to compensate for the residual positional drift. One method is based on the use of a priori knowledge, by previous measurements of the focal spot position during time, which are then used for predicting and compensating for the errors in future XCT measurements ([38],[218]). A second method is based on the direct measurement of the temperature at the source and on the assumption of a correlation between the temperature and the drift ([137],[283]). Another method is based on acquiring, together with the rotating object being XCT scanned, additional stationary reference objects (e.g. spheres) which can be used to determine the positional drift directly on the X-ray images (see Fig. 12 and [216]).

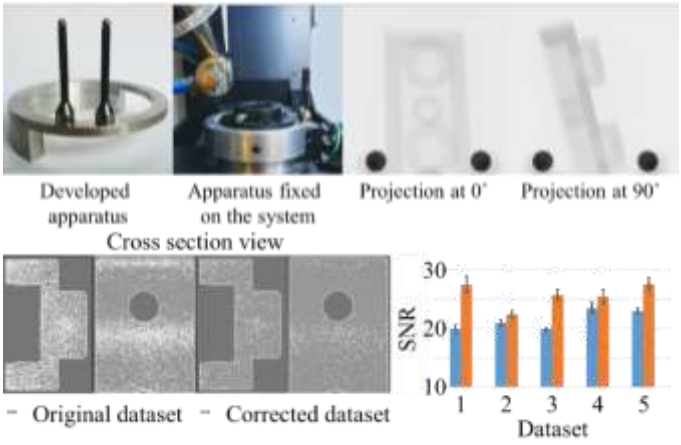

Fig. 12. Compensation of focal spot drift using stationary reference spheres. (top) experimental set-up; (bottom left) reconstructed datasets before and after correction; (bottom right) Improvement of Signal-to-Noise Ratio for five experimental runs [218].

2.3 Detectors

The characteristics of the X-ray detectors are fundamental for the quality of the X-ray projections and, consequently, of the reconstructed XCT volumes. Many different detector solutions are available, ranging from linear (1D arrays of pixels) to flat-panel detectors (2D pixel array), and from energy-integrating (i.e. producing a signal that is nominally proportional to the total energy of all photons deposited within the readout time) to photon-counting detectors (which also register spectral information, enabling material decomposition by so-called spectral XCT) [248]. Details on the different types of detectors, as well as on their capabilities and limitations, are available elsewhere [63]. Most industrial XCT systems are cone beam systems using a flat-panel energy-integrating detector that, in

most cases, consists of a scintillating layer that converts the X-rays into visible light, which is subsequently sensed by a photodetector (see Fig. 13). The topics discussed in this section mainly refer to flat-panel scintillation detectors.

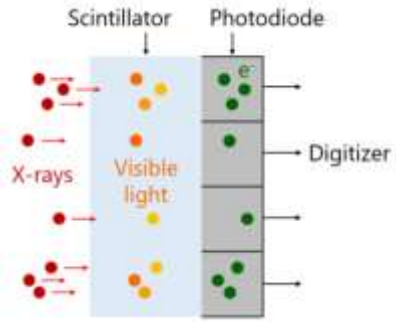

Fig. 13. Schematic representation of the principle of a scintillation detector [94].

The image quality of the projections, and hence of the XCT reconstructions, is dependent on several detector characteristics, including number of pixels, pixel size, geometric distortions, detection efficiency (i.e. geometric efficiency and quantum efficiency), afterglow and internal scatter, pixel cross sensitivity, response time and image lag, dynamic range, burn in, and stability over time. More detailed information on the detector characteristics can be found elsewhere ([63],[68]). In the following, some of the key detector characteristics are introduced, along with methods for characterizing and correcting them.

X-ray detectors often have between 1000×1000 and 4000×4000 pixels. Depending on the number of pixels, to achieve high resolution, and hence small voxel size, in cone-beam XCT the magnification factor should be sufficiently high, compatibly with the size of the investigated sample or part. Therefore, a trade-off is required between the voxel size and the field of view (FoV), although other solutions are possible using the stitching of multiple reconstructed images [170]. Detecting small features (such as small topographic features) can be a challenge in the typical FoV of medium sized manufactured components. In such cases, a possible solution is given by local (region of interest) tomography. Scans performed with material outside the FoV can introduce significant imaging artefacts yet methods exist to compensate; this allows good reconstruction of the geometry within the region of interest, although shifts in the contrast values are possible ([42],[171],[299]).

Geometric distortions, i.e. deviations in the actual sizes and positions of the detector pixels, can result from problems due to the single components of the detector, as well as from the detector mounting and stability. To achieve accurate reconstructions, procedures have been developed to characterize and correct such distortions. For example, Weiss et al. [288] acquired X-ray projections of a calibrated grid at several in-plane orientations of the detector. An error separation approach was used to discriminate errors caused by in-plane distortions of the detector from misalignments and deviations of the grid. A detector distortion map was then obtained (see Fig. 14), which allowed re-binning of the subsequently acquired projections, thus correcting the determined in-plane distortions prior to reconstruction. A more recent study by Lüthi et al. [187] separated in-plane detector distortions from out-of-plane distortions (that are also called detector topography) placing a calibrated ball plate close to the detector to acquire X-ray projections at different detector positions along the magnification axis, i.e. at different SDDs. Lüthi et al. found flatness errors of approximately 1 mm, which they attributed to stresses originated by the detector mounting. The maximum distortion due to the flatness error was 0.95 pixels for an SDD of 1 m, and it increased for lower SDDs. Additional distortions of up to 0.15 pixels originated from detector temperature variations of up to 3 °C, confirming that appropriate temperature control of the detector can be critical for accurate XCT measurements (see Section 2.4).

Spatial non-uniformity and non-linearity in the output of the detector is influenced by several factors, including energy- and geometry-dependent phenomena in the detector, thickness variations in the scintillator, and background signals ([22],[160]). The overall signal and noise performance of a detector can be described by its detective quantum efficiency, measured according to IEC 62220-1 ([106],[136]). The latter typically ranges from 2 % to 50 % depending on the spatial frequency considered [256]. Fourier transform based metrics, such as the noise power spectrum and MTF, provide more complex indications of image quality [130]. Image lag, causing loss of contrast and resolution, is attributed to three steps in the detector operation: afterglow in the scintillator, trapped charge in the photodiode matrix, and incomplete readout of the photodiodes [122].

X-ray intensity qualification of flat-panel detectors generally includes two corrections: the defective pixel correction and the intensity variation correction. The defective pixel correction, also called “bad” pixel correction, can be performed by acquiring a number of X-ray images taken with the free detector (without pre-filters and objects in the FoV), which are then used to determine a map of the defective pixels; corrections to the identified bad pixels are then based on the mean of the neighbouring good pixels [63]. The intensity variation correction includes flat-field, dark-field and gain corrections. The flat field correction compensates for shading due to inverse square dropoff of X-ray intensity from the central beam axis. Before applying flat-field or ‘shading’ corrections, zingers (i.e. random events of emitted radiation [262]) need to be identified and removed, e.g. by determining the differences in the intensities of the corresponding pixels in two or more images acquired at nominally equal exposures. The elimination of zingers from every projection would be demanding, but it is necessary at least for those projections used in flat-field corrections, since unremoved zingers in such corrections would propagate to all projections to which the corrections are applied. Dark-field correction concerns residual detector signal when no X-rays are incident. Gain correction is used to correct for non-uniformities in the detector response, despite uniform incident X-rays. Normalized gain correction maps can be produced from observed variations in multiple images, using the same X-ray and exposure conditions (including tube voltage and filtration) as the test measurements [206]. The non-linearities of pixels response can be corrected based on multiple gain correction maps, determined at different emitted X-ray intensities, realized by piecewise ramping of the source current from zero up to the current specified for the acquisition, and then finding a gain correction function in the entire range of expected intensities, by interpolating the different gain correction maps ([169],[232]).

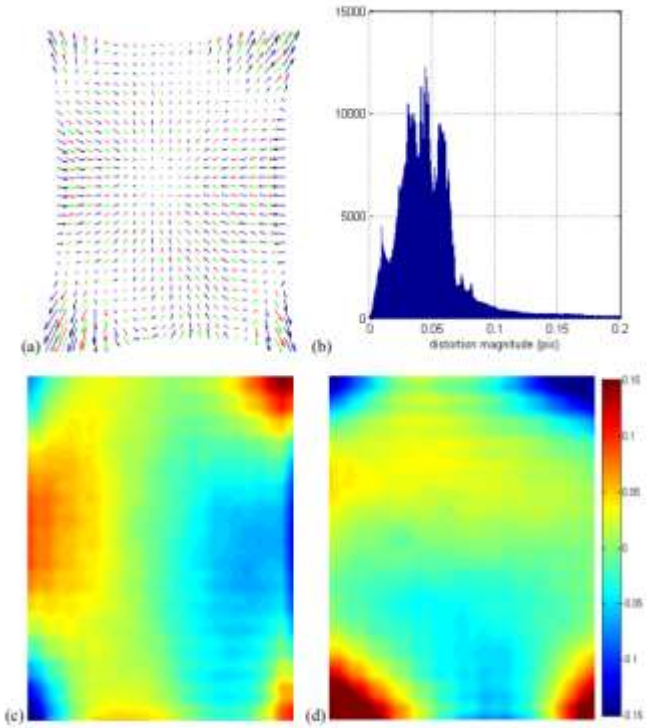

Fig. 14. Detector in-plane distortions determined from the acquisition and evaluation of X-ray projections of a calibrated grid [288] (a) Vectorial distortion map showing four independent distortion measurements shown in different colours. (b) Histogram of the distortion magnitude. (c) X- and (d) Y-components shown separately with reference to the colour-coded scale between ±0.15 pixels.

Gain corrections and their effectiveness assume that the incident intensity of the X-rays is uniform over all the pixels in the flat-field image. However, the Heel effect is a typical cause of spatial inhomogeneity of the spectra emitted by reflection-target X-ray tubes [269]. This effect produces a spatial variation in the X-ray source spectrum due to variations in the X-ray path length through the target material, resulting in a relatively higher flux of soft X-rays reaching rows at one end of the detector and a slightly hardened beam reaching the opposite rows, as illustrated in Fig. 15. Non-uniform source intensity is routinely addressed with flat-field corrections or other correction methods [304], [112]. However, such corrections may reduce the sensitivity of the detector. Therefore, new source designs can be beneficial to obtain higher homogeneity of the emitted spectrum, hence reducing the dependence on flat-field corrections and the use of hardware filters [269].

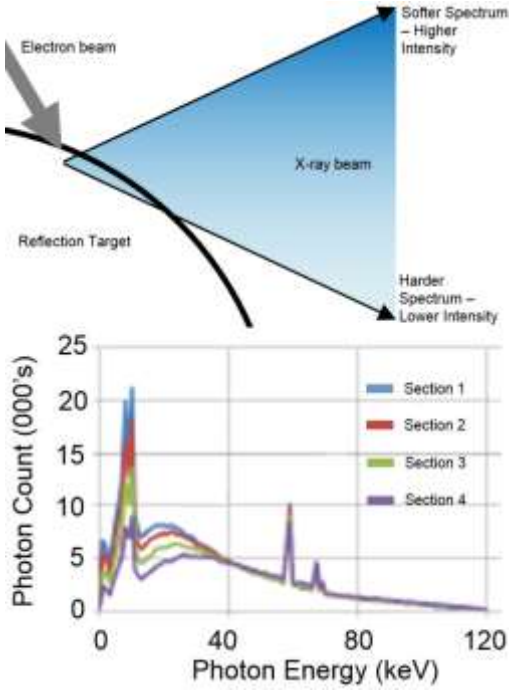

Fig. 15. Heel effect: (top) illustration of the effect produced at an X-ray reflection tube; (bottom) diagram reporting an example of X-ray spectrum variations characterised at four vertically spaced sections at the detector with Section 1 a higher ray (less penetration length hence softer spectrum) and Section 4 the lower ray (more penetration, hence harder spectrum) [269].

Properly applied procedures for detector pixel correction and intensity variation correction can be used to eliminate ring artefacts (i.e. image artefacts that are visible in the reconstructed volumes as concentric circles of alternating contrast). When ring artefacts persist even after such corrections, they can be eliminated by other methods, e.g. by translating the detector between projections during acquisition [72] or, more commonly, by applying software corrections during reconstruction [111] (see also Section 4.3).

The imaging system is subject to drift, as the X-ray intensity at the detector is unstable over time. This instability is predominantly caused by thermal effects and, to a lesser extent, by unstable magnetic focusing inside the X-ray source (see Section 2.2). Periodic monitoring of the imaging system is used to mitigate the effects of such temporal instabilities. Gain corrections performed before and after scanning, and possibly their interpolation over the scan time, can be used to control drifts in gain correction maps. Thermal heating of the detector components produces electronic noise and an offset of the pixel intensities (dark current), which can be mitigated through background subtraction (i.e. subtraction of a mean offset image determined from various raw radiographic images acquired without X-ray illumination [292]) and through temperature control (see Section 2.4).

2.4 Environmental conditions

Temperature is one of the major influences in dimensional metrology in general. In XCT, temperature can be even more critical than with other coordinate measuring systems (CMS), since XCT systems include significant heat sources, primarily the X-ray tube (which dissipates approximately 99 % of its energy into heat – see Fig. 2), in addition to the detector (which may dissipate heat of the order of 100 J/s [40]), motors, drives and electronics. Furthermore, temperature variations can yield multiple direct and indirect influences on the XCT dimensional measurements: thermal expansion and deformation of the workpiece and of the

machine kinematics, drift of the focal spot (see Section 2.2) and changes in the detector response (see Section 2.3). Traceable and accurate measurements require thermal stability of both the XCT system and the workpiece, as well as solutions to correct or eliminate the deviations from the standard temperature of 20 °C and the thermal gradients and transients (which can induce critical effects such as geometrical distortions).

Thermal studies have been performed on the X-ray tube [100], cabinet [122] and detector [40]. For example, to ensure the long-term stability needed for a sub-micrometre precision metrological XCT system, METAS developed a temperature control system managing all heat sources within the radiation shielded cabinet, comprising air conditioning, three individual water-cooling circuits and thirty calibrated temperature sensors used for monitoring and numerically compensating for thermal expansion [41]. Good practice is to place thermal sources, such as motion controllers and power supplies, outside the cabinet whenever possible. The heat generated by the X-ray tube and the detector can be removed by liquid cooling systems; otherwise, if only managed by the air conditioning, the temperature increase would be of several degrees Celsius, as demonstrated by experiments carried out at METAS [37]. Traditional X-ray tubes are actively cooled to avoid target damage; nevertheless, allowing the XCT system to reach a stable temperature before starting a high-precision measurement is often essential (see Section 2.2). Water-cooling of the detector is not common but has been recommended for metrological applications [40]. Temperature has a significant impact on the detector performance (see Section 2.3). Kuusk [168] reported dark signal deviations of up to 10 % for 1 °C detector temperature variations. METAS [40] developed an efficient shielded detector water-cooling system that keeps the detector mean temperature at 19 °C, as opposed to the 29 °C reached without active water-cooling. The main advantage of an optimised water-cooled detector is that it not only minimizes the heat flow into the XCT system and the consequent thermal and geometrical variations, but also strongly reduces start-up times and stabilizes dark currents and pixel gains (see Fig. 16).

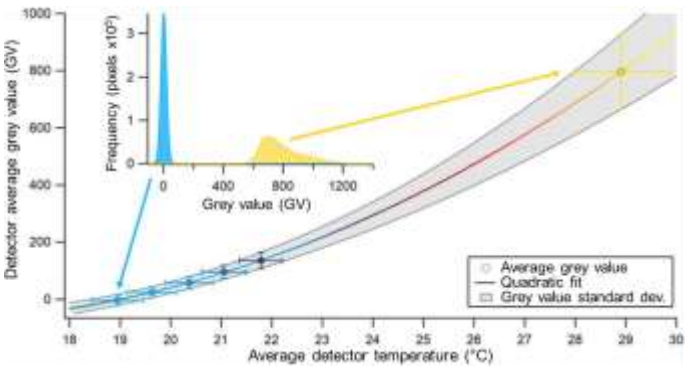

Fig. 16. Average dark grey value across all detector pixels relative to the detector average temperature; error bars indicate grey value (vertical) and temperature (horizontal) standard deviations across the detector [40].

Other environmental factors are normally less critical than temperature. Mechanical vibrations induced from the air-conditioning or from other external disturbances can reduce the precision of XCT results (e.g. due to augmented noise) or can impair the success of measurements (e.g. due to motion artefacts resulting from sample instability). Cuadra et al. [70] and Panas et al. [210] proposed methods to evaluate the measurement uncertainty for a single voxel using a measurement model which quantifies acquisition-specific noise parameters, including mechanical vibrations. Humidity is another environmental factor which may influence measurement uncertainty, e.g. through material expansion, especially for polymeric parts [55]. A further factor is environmental scattering, which depends on the characteristics of the X-ray beam and its cone angle, as photons missing the workpiece may be deviated by components that are within the environment of the XCT system cabinet. Investigations show that environmental scattering can contribute significantly to the total scattered radiation ([192],[237]).

3. Influence factors related to workpiece and XCT device settings

This section covers influence factors that are directly controlled by the XCT device operator as a function of the workpiece properties. It concerns more specifically X-ray source settings (Section 3.1), workpiece position and orientation (Section 3.2), and number of projections (Section 3.3). Finding the task-specific optimal combination of all settings remains a challenge. Therefore, a brief review of optimization procedures and a note on the influence of further workpiece properties are provided in Section 3.4 and 3.5 respectively.

3.1 X-ray source settings

The spectrum emitted by the X-ray source is strongly dependent on the source settings and target material (Fig. 17). Metal targets with low atomic mass, such as copper and molybdenum, primarily produce low-energy X-ray photons, hence are preferred for imaging low X-ray absorption materials, such as polymers [157]. Tungsten is preferred for highly absorbing materials, as it produces a larger share of high-energy photons and has a relatively high melting point (see Section 2).

The electrical current running through the tungsten filament (Fig. 2) determines the number of electrons emitted due to the thermionic effect, hence the photon count and the eventual contrast-to-noise ratio. Care needs to be taken when selecting the source voltage and current to ensure that the detector is not saturated, as this can negatively impact its long term operation.

The acceleration voltage applied between anode and cathode in the X-ray tube influences the emitted photon energies, with the maximum photon energy being proportional to the acceleration voltage. Therefore, the voltage determines the maximum penetrable material thickness (See Table 1) while also influencing contrast. If the tube voltage is too low for a given measurement task, then there will be one or more X-ray trajectories in the acquisition that will succumb to insufficient photon transmission through the workpiece, a phenomenon known as photon starvation. The result is an extremely low signal-to-noise ratio for the corresponding projection intensities and subsequent creation of so called extinction artifacts in the reconstructed image.

The polychromaticity of the photon spectrum is an important cause of image artefacts. Conventional FBP reconstruction algorithms presume energy-independent attenuation, despite attenuation being an energy-dependent phenomenon (see the variable E for energy in the Beer-Lambert law, equation 1). The consequence of this discrepancy between the polychromaticity of the acquisition and the monochromaticity presumed by the reconstruction algorithm is the creation of so called beam hardening artifacts (see Section 4.1). Hardware filters, typically metal plates, can be placed in front of the source to attenuate low-energy photons, hence narrowing the spectrum.

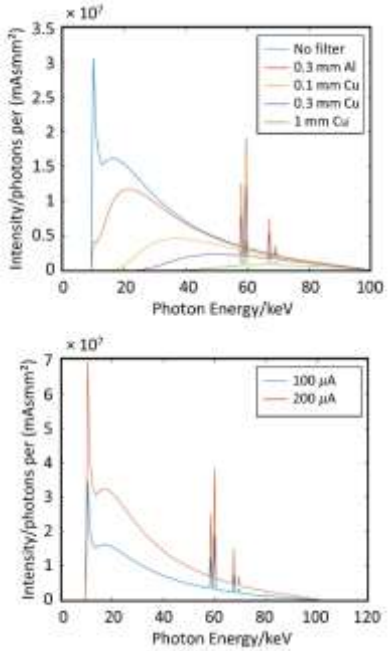

Fig. 17. Influence of source settings on the X-ray spectrum [213].

Table 3
Length measurement errors on full image width induced by measured energy-dependent deviations in detector and focal spot positions [134].

Deviation	Geometrical magnification		
	2	10	50
50µm detector shift due to voltage U	10 µm	2.0 µm	0.4 µm
100 µm detector shift due to filter	20 µm	4.0 µm	0.8 µm
10 µm source shift due to voltage U and filter	2.0 µm	3.6 µm	3.9 µm

The actual spectrum emitted by the source can be measured using photon counting detectors [260]. This, however, bears the drawbacks of experimental setup changes as well as of excluding the original detector response. Another approach relies on estimating the spectrum based on transmission measurements of e.g. a step wedge by using expectation-maximization or truncated singular value decomposition algorithms [243], [58].

Recent research has emphasized additional complexity related to spectrum-dependent source and detector positions in XCT (Fig.18). Tube voltage, filter material and workpiece material, all of which change the spectrum incident onto the detector, were each reported to induce variations of 50 µm to 100 µm in effective penetration depth for a 600 µm thick CsI scintillating layer ([133],[134]). Similarly, due to the Heel effect (See Section 2.3), the effective position of the focal spot of the full polychromatic beam differs from the effective focal spot position of a hardened X-ray beam after hardware filtration ([133],[134]). Indications of the potential influence on dimensional measurements as a function of magnification are listed in Table 3.

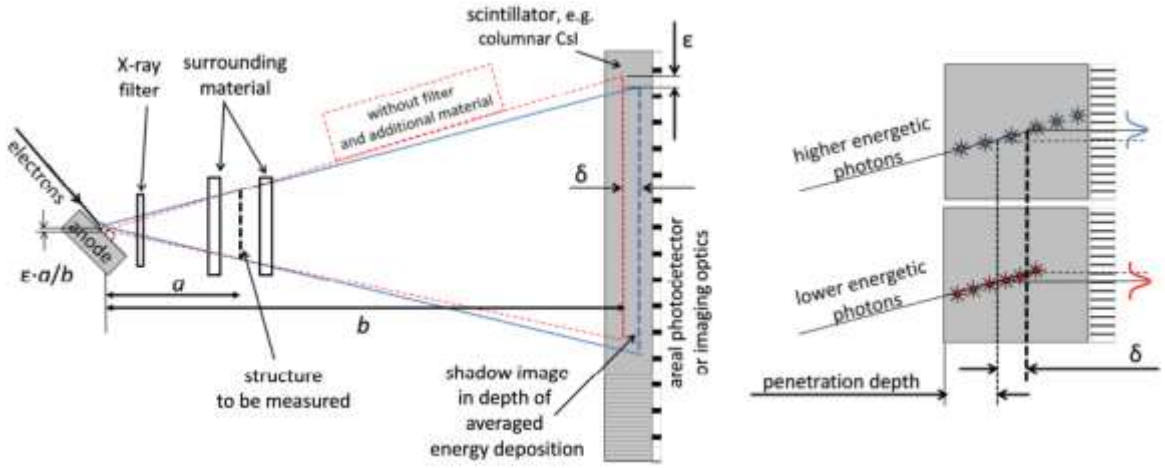

Fig. 18. Energy dependence of effective focal spot and detector positions [133].

3.2 Workpiece position and orientation

The positioning of the rotation stage along the magnification axis determines the geometrical magnification, hence the voxel size of the reconstructed model, and has a significant influence on the structural resolution [306]. In most cases, magnification is maximized within the limits of detector coverage. Large magnifications enable measurement of small features and topographical details, sometimes outperforming optical techniques, such as confocal microscopy [307]. Nevertheless, Thompson et al. have reported an optimal magnification for surface topographical measurements at 20× magnification with bias increasing at smaller and larger magnifications and repeatability consistently decreasing at higher magnifications [266]. This degradation can be attributed to multiple effects, including additional noise due to increased X-ray flux per unit volume, increased scatter, and focal spot induced blur. Magnification is moreover limited by the focal spot size, since voxel sizes smaller than the focal spot size yield blurring [256]. Villarraga-Gómez showed that larger magnifications are associated with reduced bias and uncertainties for bidirectional measurements and form measurements (Fig. 19) [275]. Uni-directional length measurements were less influenced by the magnification.

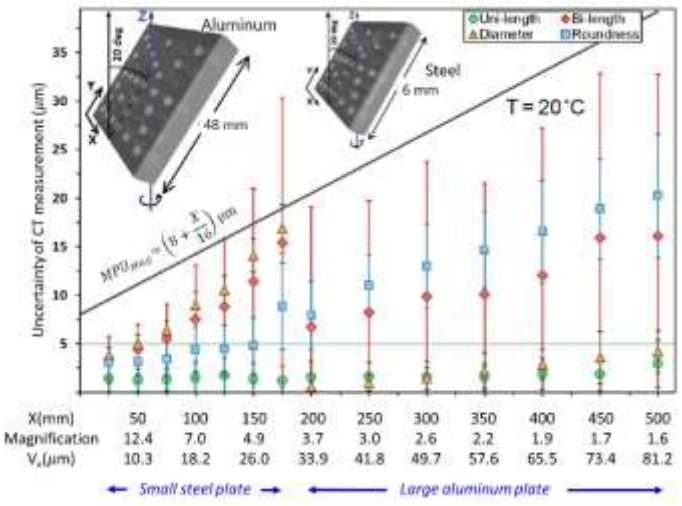

Fig. 19. Influence of workpiece magnification on measurement uncertainties [275].

The orientation of the workpiece in the XCT device influences the required source settings, as well as the presence of scatter, beam hardening and Feldkamp artefacts in the reconstructed volume, hence the accuracy and precision of the XCT dimensional measurements ([113],[279]). Moreover, orientation determines potential mounting strategies, which in turn influences stability hence measurement uncertainty [231]. Feldkamp artefacts occur since circular acquisition trajectories do not satisfy the Tuy-Smith data sufficiency conditions, which implies that the commonly used filtered back projection method for reconstruction (Section 4.2) is only approximate except from the central slice [270]. Particularly for large cone beam angles, this approximation yields Feldkamp artefacts visible as smeared and noisy surfaces, hence increasing the apparent form error of the surface. As a general rule, planar surfaces should, therefore, not be oriented perpendicular to the scanner's axis of rotation. In a case reported in [7], optimal orientation of the workpiece could reduce the workpiece surface area affected by Feldkamp artefacts from 23 % to 0 %. Alternative scanning strategies, such as helical scanning, can also eliminate Feldkamp artefacts ([4],[120]). An optimal scanning orientation moreover minimizes the variance of the traversal path length throughout the workpiece during the scan. An extensive experimental study on the influence of workpiece orientation has been reported in [279] for a set of objects sized between 5 mm and 70 mm. The authors conclude that, especially for form measurements, an optimal orientation can reduce deviations compared to tactile measurement results by 40 % to 70 %.

3.3 Number of projections

The number of projections has a major influence on the structural resolution of the reconstructed image, which is particularly important when studying pore size, morphology and distribution, e.g., in an additively manufactured part ([85],[211]). Reconstructions performed from an insufficient number of projections yield view aliasing visible as streaks emanating from sharp edges in the reconstructed volume [152]. The minimum number of projections required for an optimal reconstruction result is directly related to the Nyquist-Shannon criterion. For a detector row coverage of M pixels, the theoretical minimum number of projections equals $\pi \cdot M/2$ [54]. Nevertheless, acquiring fewer projections can also yield acceptable results, while reducing the acquisition time ([277],[287]).

Sinogram interpolation can be used to virtually increase the number of projections of undersampled scans with the aim of increasing speed while limiting view aliasing artefacts and loss of structural resolution [110]. Körner et al. [161] have shown sinogram interpolation based on 40 % to 60 % of the theoretically required number of projections to yield promising results for characterizing surface topography at significantly reduced scanning times. Other approaches are currently under development that rely on either machine learning approaches ([212],[297],[298]) or that employ prior-knowledge in the form of a CAD-model as additional information to compensate for a reduced number of projections. In the latter case, iterative reconstruction methods ([31],[33],[249]) or machine learning based approaches [88] are preferred over conventional filtered back projection.

3.4 Optimization procedures

The optimal combination of XCT device settings remains a challenging task that is largely based on experience and expert judgement, leading to large variations as illustrated in Fig. 20. Often, extensive experimental studies relying on Design of Experiment approaches are performed in order to determine an optimal combination of scan settings, e.g. ([85],[211],[266]).

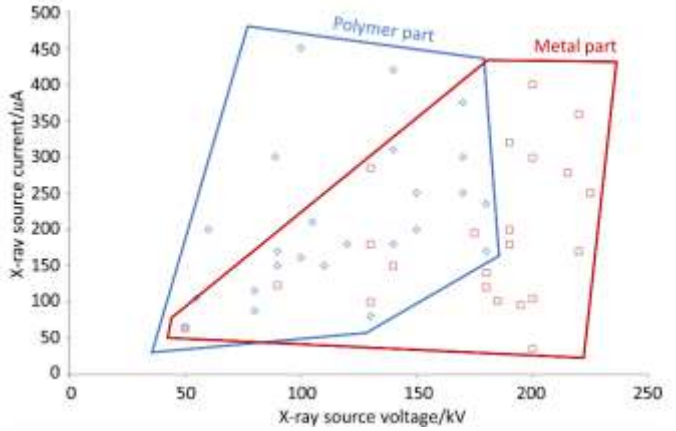

Fig. 20. Selection of X-ray source settings of two parts by twenty experienced operators (based on [13]).

An approach to identify a minimal number of projections yielding a sufficient reconstruction quality based on frequency analysis has been proposed in [51]. The optimal orientation of a workpiece can be found based on its CAD model and analysis of associated tolerances. Computationally efficient methods have been developed that enable identification of surface regions that cannot be accurately reconstructed under given orientations ([7],[108],[113],[301]). Ray tracing furthermore enables the prediction of the variation and maximum of the transversal path length during a circular scan. Research on the optimal way of combining Feldkamp artefact reduction and transversal path length criteria has hitherto not yet been performed [279].

There have been studies on a number of user support systems aimed at identifying optimal combinations of user settings without the need for extensive simulations. Schmitt et al. [234] propose a case-based reasoning system that identifies similarities between a workpiece CAD model and cases stored in a database for this purpose (Fig. 21). Giedl-Wagner et al. [103] rely on machine learning for identifying similarities. However the need for a large training dataset, combined with the need for associated reference measurements, hinders the practical applicability of the approach [230].

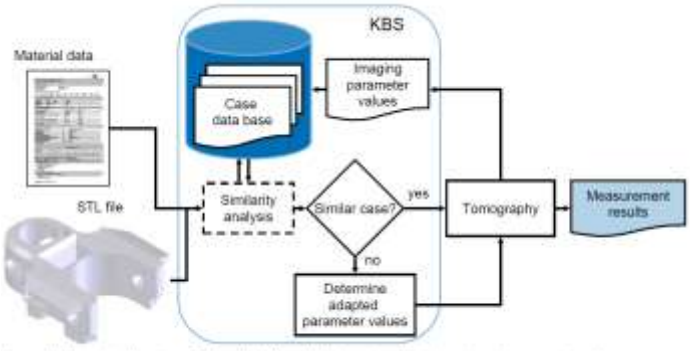

Fig. 21. Structure of knowledge-based system to predict adequate setup parameter values [234].

3.5 Workpiece

The influence of workpiece properties on the eventual measurement result is significant and covered throughout this paper. Attenuation properties of the workpiece material, in combination with the workpiece size and geometry, influence source settings, beam hardening, scatter, among other effects. The complex dependence of XCT measurement deviations on the workpiece properties complicates, e.g., the definition of suitable reference objects for generic acceptance testing, as described in Section 5 [28].

In addition, surface texture also influences bias between XCT measurements and tactile measurements, which are often considered as reference. Several authors have experimentally determined such bias for turned [43], sandblasted [233], cast [25], or additive manufactured parts [3], and demonstrated successful compensation. The surface texture parameter *Rp* was suggested as a generalizable offset of the XCT least-squares surface [62], but more research is needed here.

4. Influence factors from the CT data processing pipeline

The conventional XCT data processing pipeline for performing dimensional measurements comprises the reconstruction of a 3D grey value model from the set of acquired projections (Section 4.1), followed by surface determination (Section 4.2) and final measurement (Section 4.4). In between, optional data enhancement steps can be applied (Section 4.3). The following sections provide a review of the different steps with particular emphasis on the influence on measurement performance.

4.1 3D reconstruction

XCT requires the reconstruction of a 3D voxel model from the acquired 2D projections, where each voxel in the model is characterized by a grey value representing the local X-ray attenuation. The most common approach to tomographic reconstruction from 2D projections acquired from a circular trajectory use the Feldkamp-Davis-Kress (FDK) algorithm, which is an extension of the filtered back projection (FBP) algorithm to cone-beam geometry [89]. To reduce noise and avoid image blur due to discretized sampling, filters, such as ramp, Hanning, cosine, Butterworth, and Shepp-Logan, are applied row-wise to the projections prior to back projecting [63]. On low-noise datasets, all filters reportedly result in similar reconstructions and thus measurement results [255], though Hamming and cosine filters have a tendency for reducing structural resolution by as much as 20 %, when compared to ramp filters, due to high-frequency cut-offs [46]. Conversely, these filters yield better performance on noisy data sets.

FBP based algorithms suffer from a number of reconstruction artefacts due to the underlying approximations [184]. FBP reconstruction is known to suffer from beam hardening artefacts, due to the assumption of beam monochromaticity. Since low-energy photons are more readily absorbed than high-energy photons, this leads to e.g. cupping artefacts overemphasizing the grey values at the edges of the reconstructed workpiece, or streak artefacts between highly absorbing object regions (Fig. 22). Placing a hardware filter in front of the X-ray source narrows the beam spectrum and reduces beam hardening artefacts. Beam hardening correction by software is common and remains a field of intensive research (Section 4.3). The recent development of photon-counting detectors, which preserve the energy information of each photon, is also promising; high-energy thresholding can subsequently be used to select a narrow band of measured photon energies used for reconstruction [80].

As indicated in Section 3.2, FBP reconstruction based on circular acquisition trajectories yields cone beam artefacts. For example, the sphericity deviations of the spheres shown in Fig. 23 are up to five times higher at the polar regions, which are affected by cone beam artefacts. Strategies investigated to reduce cone beam artefacts include the use of non-circular scanning trajectories (e.g., helical scanning), correction during reconstruction ([11],[23], [104],[107],[165]), or iterative reconstruction methods (see below).

Considerable research efforts have been dedicated to the development of alternatives for FBP by means of iterative reconstruction algorithms that exploit the continuously increasing computational power. Based on an initial estimate of each voxel's attenuation value, simulated forward projections are compared to acquired projections leading to a subsequent update of the estimated attenuation values. This procedure is iterated a predefined number of times or until a mathematical condition is met. Assuming sufficient computation power, iterative reconstruction methods have the inherent capability to consider the polychromatic nature of the X-ray beam, finite and inhomogeneous focal spots, misalignments and scatter [33].

Research is being devoted to the development of novel reconstruction methods for non-conventional sets of projections. Such research concerns, e.g., incomplete circular trajectories comprising only a limited set of projections ([36],[220],[244]) or even fully flexible robot XCT scans ([125], [155],[172]). Methods are being proposed that enable task-specific identification of the set of projections for optimal scan results either before ([47],[98],[115]) or during the scan ([32],[71]).

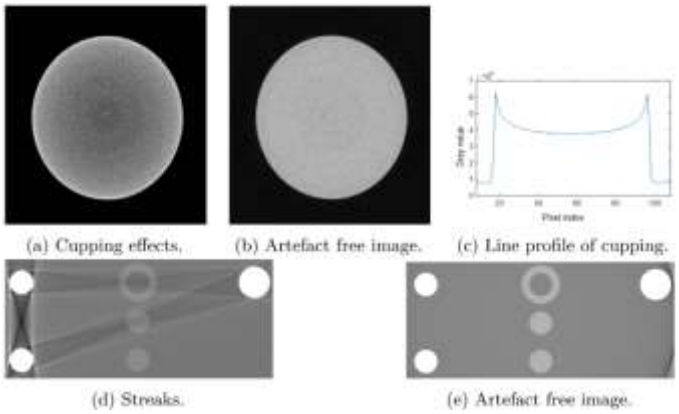

Fig. 22. Beam hardening artefacts: cupping artefact (top) and streak artefact (bottom) [57].

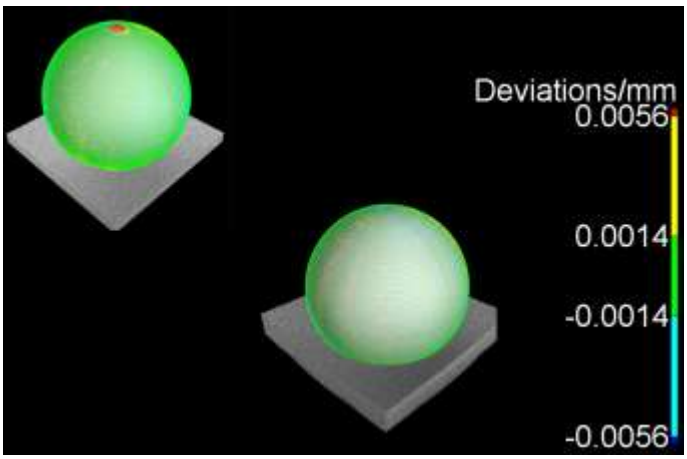

Fig. 23. Fit point deviations of an 8 mm sphere with (left) and without (right) cone beam artefacts at the polar regions (Courtesy of PTB).

4.2 Surface determination

The XCT reconstruction step discussed in the previous section yields a 3D grey-value model, where the grey value of each voxel is ideally representing the X-ray attenuation at the voxel position. A combination of effects (e.g. partial volume effect, beam hardening, scatter, misalignments, finite focal spot) complicates the identification of the eventual edge of the investigated components, especially in the case of multi-material components with complex geometries [46].

The algorithm used for surface determination has a direct influence on bidirectional dimensional measurements, and in case of low-quality scans or non-symmetry, also an indirect effect on unidirectional measurements. Nevertheless, segmentation accuracies reaching below 10 % of a voxel size have been reported for mono-material objects under optimal scanning conditions ([10],[222]). The influence becomes particularly strong in the case of complex 3D geometries with varying X-ray penetration lengths, where both artefact removal and the definition of the measurand become non-trivial. In these cases, surface determination becomes one of the most influential factors contributing to the eventual measurement uncertainty [267].

A growing variety of segmentation methods is being used, including global thresholding algorithms that employ a single grey value threshold for the entire volume, such as ISO-50 % or Otsu [208]; local adaptive thresholding algorithms that rely on an assessment of grey value gradients ([59],[302]), or region growing starting from a seed until a homogeneity criterion is no longer met [35]. An extensive discussion and quantitative performance evaluation of thresholding techniques used for nondestructive testing and image applications is available from [239]. Repeatability of segmentation steps reported in literature is high [253]. Local iterative surface determination has been shown to be more accurate compared to global thresholding methods for both geometrical measurements of mono- and multi-material objects [46] and surface texture parameter generation [268] for high-quality scans. The eventual surface detection of local adaptive thresholding as available in commercial software implementations has been shown to be robust, though conflicting results have been reported on the influence of the chosen starting contour; hence, further research is required ([46],[124]).

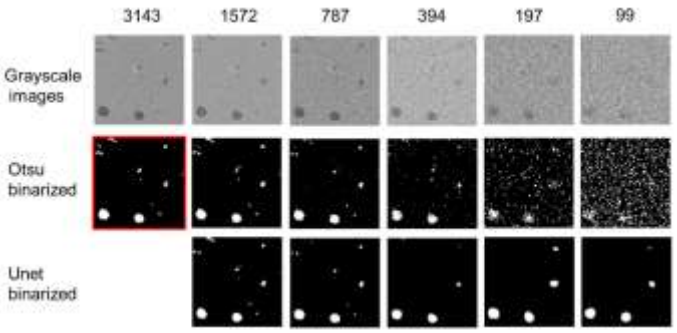

Fig. 24. Effect of number of projections and chosen segmentation algorithm on porosity detection. (top) grey-scale images based on a number of projections decreasing from 3143 to 99. (middle) Binarized images using Otsu segmentation. (bottom) Binarized deep learning segmentation (based on [34]).

Recently, deep learning-based segmentation is gaining attention. This form of segmentation concerns, in particular, methods to identify and segment, e.g., defects, pores or fibres in noisy data sets ([34],[159]). An example of the potential performance of such methods is depicted in Fig. 24.

4.3 Artefact correction and noise reduction

Throughout the data processing chain, algorithms are applied to reduce noise and artefacts, and to enhance the data quality. Corrections and enhancements applied to the projections are aimed at avoiding the need to propagate the corresponding errors. Such algorithms concern, e.g., corrections for defective pixels, pixel intensity variations, source drift, and geometric distortion of the detector, as discussed in Section 2.3. Reduction methods for major artefacts, such as those due to beam hardening and scatter, and noise are targeted at different stages: prior to, during, and after reconstruction.

Noise can have an important contribution to measurement uncertainty due to its influence on the segmentation of the XCT volume. While the influence on, e.g., sphere centre-to-centre distance measurements remains limited due to averaging over many points captured on the spheres, probing errors are widely believed to be more strongly influenced by noise. An overview of quantities influencing XCT image noise and of metrics used for assessing noise in XCT can be found in [223]; see also Fig. 25. Quantum noise is influenced by source settings, object properties and placement, and detector characteristics. Detectors can add variable levels of electronic noise. The eventual noise in the XCT image strongly depends on the reconstruction algorithm used, with some iterative reconstruction methods reportedly outperforming FBP methods [316]. Also, the number of projections is a key contributor ([34],[277],[313]), so research targets noise reduction in the projections, during reconstruction, in the reconstructed volume model, and in the segmented surface model and point cloud. The challenge concerns reducing noise in a computationally efficient way, while preserving edge information and not compromising structural resolution [26]. An in-depth discussion on the applicability of different filters in the medical domain is available from [271]. Overall, better trade-offs between noise reduction and structural resolution are reported when reducing noise during and after reconstruction, as compared to pre-reconstruction filtering [16]. For example, Bartscher et al. [26] show that applying a 2D 3 × 3 median filter on the projections is promising but does not perform as well as filtering during or after reconstruction. Rodriguez-Sanchez et al. [223] conclude that a predictable correlation between existing noise metrics and dimensional measurement uncertainty values has hitherto not yet been established, and that efforts for a combined study of noise, blur and artefacts are required, as proposed by e.g. ([185],[197]).

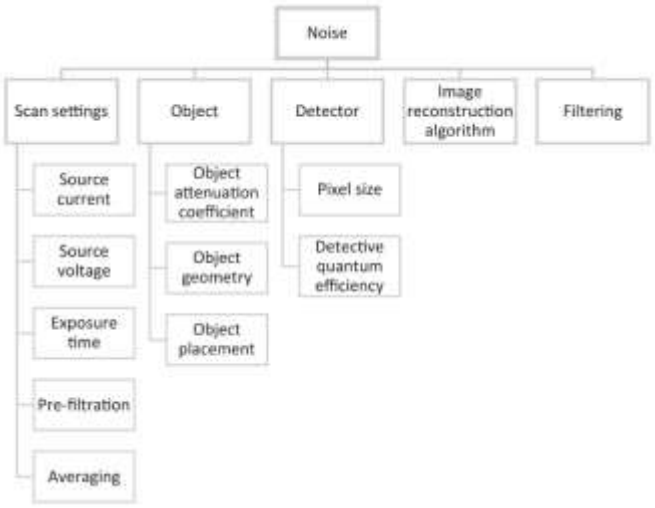

Fig. 25. Main influence quantities of XCT image noise [223].

A common software solution for beam hardening correction (BHC) is the process of linearization, which adapts the acquired projection grey values into pseudo-monochromatic attenuation data [163]. Linearization can be based on prior knowledge, such as theoretical assumptions about the spectrum and attenuation coefficients or on empirically determined coefficients using a dedicated phantom, e.g., a step wedge ([50],[65],[116],[191]). Careful consideration of the transferability of presumed polynomial coefficients for the envisaged linearization is required, since deviating coefficients rapidly worsen eventual measurement errors ([56],[74]). Other approaches require no prior knowledge but are based on iterative optimization via repeated reconstruction and forward projection ([127],[151],[226]). Such approaches are currently less applied industrially due to high computational demands. Kachelriess et al. proposed a referenceless BHC strategy based on cupping artefact reduction, requiring only N+1 reconstructions for an N^{th} order polynomial linearization [153]. For objects consisting of multiple materials with strongly deviating attenuation coefficients, dual energy methods have been proposed ([6],[251]). These methods require two scans of the workpiece at distinctly different settings. Comparisons of different BHC methods for multi-material objects have been published ([27],[56],[183],[221]). It can be concluded that strong beam hardening effects risk leading to measurement deviations of up to three times the voxel size for geometrically simple objects, which can be reduced by adequate BHC by a factor between three and ten. For complex geometries, edge detection can be severely limited by beam hardening artefacts leading to considerably larger deviations if not corrected.

Since Compton scattering represents a dominant X-ray attenuation mechanism in common industrial XCT applications [166], the presence of scattered photons onto the detector is somewhat unavoidable. Moreover, detector-internal scatter has been shown to yield important additional contributions to the overall scatter signal [236], followed by radiation scattered by the device enclosure. Filters, beam collimation and collimated linear detector arrays are hardware solutions to reduce scatter, though the latter comes at the expense of severely increased scan time requirements. Common software-based scatter correction strategies rely on a second set of projections acquired in the presence of either a beam stop array (BSA) yielding zones with only scatter information, a beam hole array (BHA) yielding complementary zones with nearly only primary signal, or a modulator with an equidistantly spaced pattern (Fig. 26). Hence, estimated scatter contributions are subtracted from the projections before reconstruction. In order to avoid the need for an additional set of projections, methods have been developed that use a moving modulator [235] or beam stopper ([303],[314]). Projection data that is missing due to the presence of the beam stoppers is then estimated using interpolation. Software methods are based on the deconvolution of the scatter affected projections by a scatter kernel generated either empirically or through CAD-based Monte-Carlo simulation ([179],[258],[263]). More recently, machine learning based approaches are being developed ([138],[180]). A comparison between different scatter correction methods can be found in [163]. Since scatter yields not only increased noise levels but also streak artefacts and cupping effects similar to beam hardening [128], it is essential to consider scatter in order to avoid over-correction of beam hardening artefacts [181].

Ring artefacts caused by non-ideal detector response can be reduced both in the projections – e.g., interpolating adjacent pixels or by exploiting the frequency properties of the sinograms ([202],[261],[282]) – and in the reconstructed volume e.g. ([214],[245]). A comparative study of ring artefact correction algorithms performed at different stages is available in [12].

A promising new research field is the use of deep learning for XCT artefact correction. Würfl et al. showed that reconstruction errors of limited angle XCT could be reduced by a factor of two by machine learning based determination of weights and filters for reconstruction [297]. Euler et al. successfully used deep learning techniques for reconstruction based on four projections and prior knowledge [88]. Other uses of deep learning concern blocked artefact and beam hardening correction ([57],[250],[285]) and scatter estimation [188].

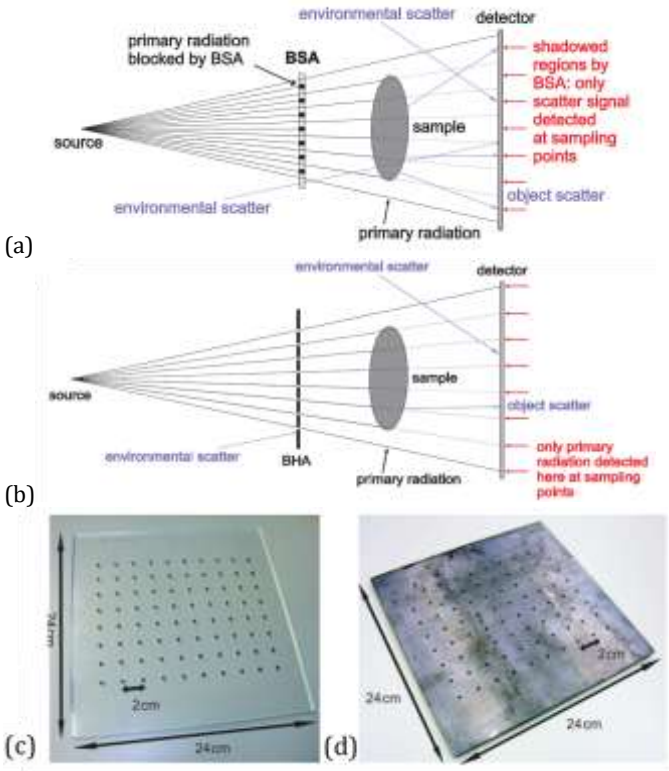

(e) 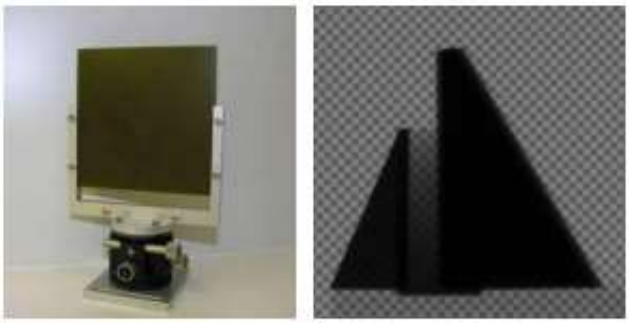

Fig. 26. Schemes of a beam-stop array (a,c) and beam-hole array (b,d) consisting of a lead sheet with small apertures placed in between source and object [236] and modulator (e) [163].

4.4 Measurement strategy

Dimensional measurements can be performed after fitting either a CAD-model or substitute features, such as planes or cylinders, onto the determined surface model. The influences of these final measurement steps have been investigated by a number of researchers, often in combination with different filtering and surface determination approaches (e.g. [124], [162], [193], [198], [200], [253]). Eventual measurement accuracy and repeatability are highly influenced by the fitting strategy chosen, especially on noisy data sets [201].

5. Performance verification

Before accepting an XCT system or any CMS, the customer performs a series of tests to verify whether the system delivers the performance stated in the specifications; this procedure is known as performance verification, while the test is called the acceptance test. Subsequently, the system performance is checked periodically – commonly to a reduced extent – by executing reverification tests [29]. It is important that acceptance and reverification tests reflect the typical use of the XCT system and encompass the entire measurement process. Verifying the dimensional measurement performance therefore requires the application of reference objects. Section 5.1 provides an overview of the current status regarding standardization. Both probing error tests (Section 5.2) and length measurement error tests (Section 5.3) are subsequently discussed. In addition, the measurement capability of an XCT device for small structures, such as edges and slits, is described by its structural resolution (Section 5.4).

5.1 Standards

At present, XCT performance verification is the subject of a German national guideline (VDI/VDE 2630-1.3) [272] and of a draft international standard ISO/DIS 10360-11 'Geometrical product specifications (GPS) — Acceptance and reverification tests for coordinate measuring systems (CMS) — Part 11: CMSs using the principle of X-ray computed tomography (CT)' [141], which has been developed by Working Group 10 (WG10) of ISO Technical Committee 213. As consensus could not yet be reached on all comments on the DIS, it was recently decided to first create a Technical Specification (TS) for performance testing of XCT systems. This TS will be based on the latest DIS version but will cover different options for some tests.

The performance verification tests should be executed under the rated operating conditions and cover all relevant error sources of the tested XCT system, as described in Sections 2 to 4. Whereas the test results characterize the 3D error behavior of the overall XCT system, they don't necessarily expose individual error sources. ISO/DIS 10360-11 describes two complementary types of tests for CMSs using XCT:

1. The local *P*-test (probing error) checks the performance of the XCT system to measure a surface locally, i.e. within a small measurement volume. The local *P*-test originally was defined to characterize the probing system of tactile CMMs [227]. The mandatory characteristics "probing form error All" ($P_{\mathrm{Form.Sph.All}j\mathrm{::CT}}$) and "probing size error All" ($P_{\mathrm{Size.Sph.All}j\mathrm{::CT}}$) are deduced from measurements of ideally perfect spheres (or half spheres), using all measurement results, while the parameter "probing form dispersion error" ($P_{\mathrm{Form.Sph.D95\%}j\mathrm{::CT}}$) is based on using 95 % of the measurement data. The index *j* is a designation of material class of the probing sphere and of an obstructive body which shall be measured together with the sphere. In ISO/DIS 10360-11 the material classes *j* = Pl for class "plastic", *j* = Al for class "aluminium", and *j* = Fe for class "steel" are defined. The material class Pl is not expected to be included in the TS, as sufficiently stable reference standards are not yet available.

2. The global *E*-test (length measurement error) analyses the performance of the XCT system in the entire measurement volume. Originally it was conceived to check the translation axes of tactile CMMs [227]. The mandatory characteristic "volumetric length measurement error" ($E_{\mathrm{Vol}j\mathrm{::CT}}$) is determined from length measurements between features of spherical or cylindrical inner or outer geometries. The index *j* is again a designation of a material class.

It is expected that these two types of tests will also be included in the TS. However, the selection of mandatory and optional characteristics may still change. Moreover, characteristics may also be deleted or new parameters added in the TS.

The "maximum permissible error" (MPE) is defined in the ISO 10360 standards as the largest permissible error or deviation of a measurement from a reference quantity value. MPE values are specified in data sheets of CMSs [176]. Acceptance and verification tests check conformance with these MPE values. The proof of conformance with specifications is, however, not a mere comparison of test results with MPE values, yet needs to also consider the test value uncertainty *U*. The latter concerns the uncertainty of the determined characteristics due to the tester and the tester's equipment (e.g., reference object). The general methodology and criteria for determining the test value uncertainty are described in ISO 14253-5:2015 [142]. Important contributions to *U* are related to reference objects: e.g., calibration uncertainty, geometrical imperfections (e.g. form deviations), or incomplete knowledge of its thermal expansion behaviour. If the manufacturer data sheet does not specify operating parameters (e.g. source settings, reference object, positioning and orientation) or details on the functions used for calculating measuring points, the tester can choose these freely.

5.2 Probing Error Tests

Probing error tests rely on the measurement of (arrangements of) spheres or spherical caps (called reference standard, Fig. 27) together with an obstructive body. The diameter(s) of the reference standard must be calibrated, its surface texture and form error must be negligibly small, and the material must have suitable properties to ensure stable dimensions and an appropriate attenuation coefficient. The obstructive body is "*an uncalibrated, separate piece of material placed next to a reference standard to adjust the penetration length of the material seen by X-rays in individual projections of a CT scan*" [141]. It is made of a material of the same material class as the sphere.

Fig. 27. Werth® universal calibration sphere (left, [67]) and multi-material sphere developed by PTB (right) for testing XCT systems.

First, the unconstrained Gaussian fitted sphere of the measured sphere points is determined. Subsequently the form and size error are evaluated as follows. The "probing form error All" $P_{\text{Form.Sph.All.j::CT}}$ corresponds to the range of all radial deviations of the measured points from the calculated sphere. The range of the radial deviations of 95 % of the measured points from the calculated sphere is the "probing form dispersion error" $P_{\text{Form.Sph.D95\%.j::CT}}$. The "probing size error All" $P_{\text{Size.Sph.All.j::CT}}$ represents the difference between the measured and the calibrated sphere diameter.

Optional variants can also be determined, for instance, to increase the comparability to probing errors of a tactile CMM according to ISO 10360-5:2010 [140]. For example, $P_{\text{Form.Sph.1×25.j::CT}}$ expresses a probing form error determined from 25 measurement points on one sphere [42].

5.3 Length Measurement Error Tests

Length measurement error tests rely on measuring calibrated length standards. These can be, e.g., ball rods with two or more spheres, ball plates, gauge blocks or step gauges. These length standards are measured while located at different positions and in different orientations throughout the entire measurement volume.

According to ISO/DIS 10360-11, the largest test length should cover at least 85 % of the (theoretical) longest possible length (line segment) that can be contained in the measurement volume under test. This requirement is different from other CMS standards, which specify the largest test length shall cover at least 66 % of the longest possible length. Another difference to existing CMS standards is that in ISO/DIS 10360-11 the determination of the bidirectional length measurement error is optional. However, volumetric lengths do not include all error sources, excluding e.g. errors stemming from surface determination. Therefore, these issues may change in the TS and future versions of ISO/DIS 10360-11.

Length standards employed for the determination of the length measurement error E, as well as for determining the scale factor for system qualification, most often contain either spheres, calottes, or cylindrical features; Fig. 28 provides an overview of different length standards in use.

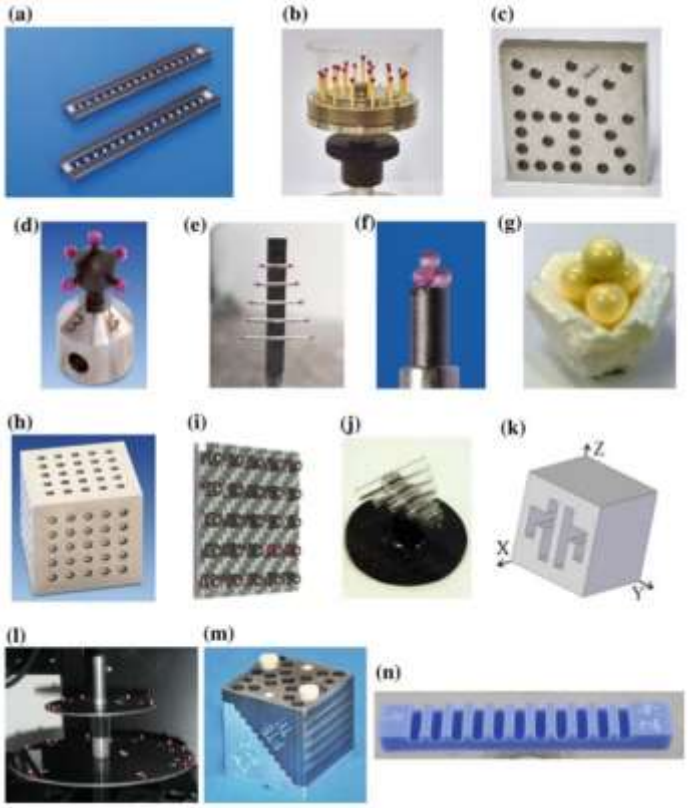

Fig. 28. Examples of length standards suitable for XCT [29] a) ball rail (Trapet Precision Engineering), b) multi-sphere standard [28], c) hole plate [28], d) star probe [21], e) CT tree [199], f) sphere tetrahedron [21], g) sphere tetrahedron [177], h) calotte cube [21], i) ball plate [199], j) pan flute standard [61], k) cactus standard [158], l) sphere disk (Courtesy of Nikon Metrology, Tring, UK), m) multi-material hole cube developed by PTB and n) miniature step gauge [55].

Fig. 29. Step cylinders: (left) standard of NMIJ, Japan with 50 mm max diameter and central bore hole [28]; (right) 250 mm standard of PTB without central bore hole ([21],[28]).

Step cylinders are applied to assess errors for different external test lengths simultaneously and can even comprise a uniform or stepped central bore hole to cover internal test lengths (see Fig. 29). VDI/VDE 2630-1.3 also discusses step cylinders with a central bore hole to study material- and geometry-dependent effects.

5.4 Structural resolution

Data obtained by XCT for dimensional measurements consist of one or more discrete sampled surfaces in 3D space. Several influence factors limit the resolution capabilities of a XCT system, which can be sorted into technological (e.g. focal spot size or detector pixel size), physical (e.g. photon shot noise), and mechanical (e.g. drift or vibrations) causes.

In the VDI/VDE 2630-1.3:2011 guideline the term structural resolution for dimensional measurements is defined as follows: it "*describes the size of the smallest structure that can be measured*

dimensionally". VDI/VDE 2630-1.3:2011 more specifically proposes to determine the structural resolution as the diameter of the smallest sphere that the XCT system can still measure within manufacturer stated error limits. Multiple limitations of this definition can be listed as: (1) it does not allow describing spatial anisotropy of resolution, (2) it is not transferrable to other CMSs, (3) it relies on the availability of a large number of spheres with different diameters, and (4) spheres with very small diameters down to common XCT system resolutions are difficult to manufacture. Therefore, two further definitions of structural resolution were proposed in [29]: metrological structural resolution (MSR) and interface structural resolution (ISR).

The MSR is derived from a single curved surface element, that is topologically described by either its local curvature or its spatial frequency components. The curvature transfer function or the MTF then describes the transition from the real profile to the measured profile and can be used to determine a single length measure denoted as the MSR for dimensional measurements. Material standards used can comprise, e.g., a reference object with local curvature or radius values (see Fig. 30) [131], or multi-wave objects ([15],[16]). The MSR statement relies on a single curved surface element, and moreover allows comparison to CMSs relying on different sensing principles.

The ISR assesses the ability of XCT to measure closely converging inner surfaces. In analogy to definitions for optical systems, it can, e.g., be defined as the minimal distance of parallel planes that can still be distinguished using a given criterion [53]. Another proposal to determine the ISR is to use two contacting spheres with known radii and to assess shape variations due to loss of resolution at the contact point of both spheres (Fig. 31) [306].

In ISO/DIS 10360-11, the two different types of resolution criteria are denoted in an informative annex as resolution type A (a form of single-sided surface resolution, single surface resolution or metrological structural resolution) and resolution type B (a form of double-sided surface resolution, multiple surface resolution or interface structural resolution). There is a technical report under development in WG 10 of ISO TC 213 to describe the resolution approaches in detail, including recent results on this topic, such as [135]. A task force was set up in ISO/TC 213/WG 10 for this purpose.

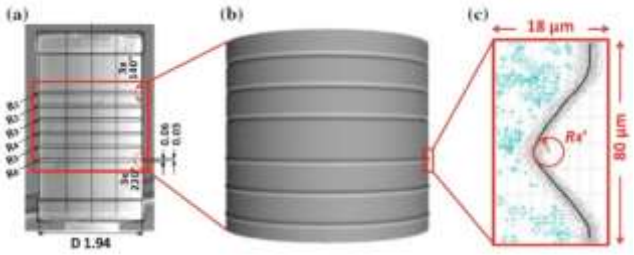

Fig. 30. Reference object for local curvature determination. a) Dimensional drawing overlaid over an electron-microscopic image, b) rendered XCT, c) exported data detail with fitted radius [29].

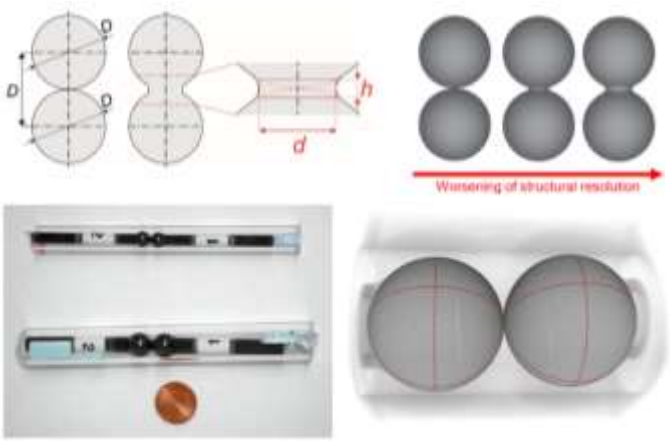

Fig. 31. (top) 'Hourglass' standard concept using two spheres for determining the interface structural resolution [306]. (bottom) Materialisation using a pair of identical ceramic spheres glued onto carbon fibre stems and XCT scan [29].

A Stedman diagram situating the performance of XCT in amplitude-wavelength space compared to other dimensional metrology techniques is shown in Fig. 32. Six XCT key parameters were taken into account to generate this diagram: the range limit of the component size, the resolution limits (in vertical and horizontal direction), and the maximum slope and minimum radius of curvature of the surface profiles [268].

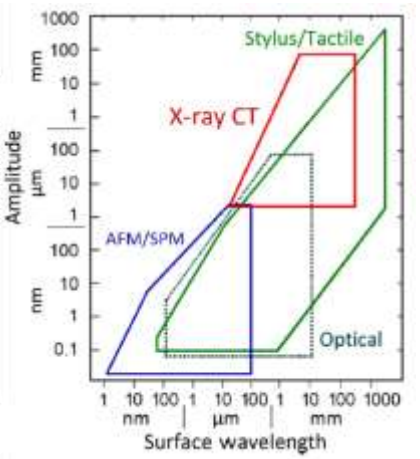

Fig. 32. Stedman diagram comparing performance of XCT with other dimensional metrology techniques [276].

6. Assessing task-specific XCT measurement uncertainty

Uncertainty is a statistical dispersion of values that can be attributed to the result of a measurement [148]. A measurement result expressed as a single value corresponding to the estimate of the measurand is incomplete without a statement of uncertainty surrounding the estimate. Uncertainty determination is a difficult task for measurements conducted with any type of CMS, even for measurement of a simple geometrical feature, e.g. a smooth sphere. Due to the multitude of influence factors (see Sections 2-4) and the complexity of many CMS probing strategies, it is often impossible to find an analytical expression for the measurement model. ISO TC 213 WG 10 has therefore developed multiple uncertainty evaluation strategies for contact CMS. However, for non-contact CMSs the development of uncertainty evaluation strategies remains an important area for further research that is reviewed here.

Demonstrating the traceability of measurements performed by CMSs remains difficult too. Formerly traceability was only

demonstrated by carrying out ISO 10360-type performance verification tests on the CMS. It is, however, important to emphasize that mere performance verification of the CMS does not imply that measurements carried out with this CMS are calibrated and/or traceable ([194],[195]). It only validates that the machine is meeting its specification with respect to measuring simple lengths, i.e., it is not generalizable to all measurement tasks. The ISO 15530 series of specification standards describes four techniques to evaluate uncertainty of measurements performed by a CMS. The first approach is based on the methods stipulated in the Guide to the Expression of Uncertainty in Measurement (GUM) [149], a second approach uses the comparator principle (often referred to as substitution method) and the third approach uses simulation [143]. There is also a fourth approach under development, namely the multiple measurement strategies method, which is outlined in the draft ISO 15530 part 2. The latter method is based on measurement repetitions performed while varying the measurement conditions (e.g. placing the workpiece in different locations in the measuring volume and oriented differently relative to the CMS axes). Use of this approach for uncertainty evaluation is limited by the feasibility of reorienting and repositioning the workpiece in the measurement volume of the CMS, and moreover presumes that a significant part of the uncertainty is repeatability of the measurement. The four approaches have been applied to XCT CMS and are reviewed here.

The GUM assumes there is a measurement model and then propagates the various influence factors for uncertainty through the model to give a final statement of uncertainty, with a statistically determined level of confidence. In XCT, determining an adequate measurement model is challenging due to the large number of influence factors, along with their potentially complex nature. Nevertheless, there have been several attempts to apply the GUM approach to XCT measurements, usually addressing elements of the process, rather than the entire measurement scenario. E.g., the sensitivity of the detection system (e.g. [75],[195]), motion systems (e.g. [194]), workpiece placement (e.g. [108]), the surface determination process (e.g. [185]) and the effects of noise (see [223]). Despite these efforts, the application of the conventional GUM approach to uncertainty evaluation in XCT remains a research challenge.

As discussed in depth elsewhere [278], the GUM usually assumes that systematic errors have been corrected where possible. There are methods available to take account of uncorrected systematic errors, but the large number of potential scenarios can make the process complex [259]. As discussed in Section 2 through 4, in XCT there are many systematic sources of uncertainty and it is rarely possible to adequately determine, quantify and correct them all (although there have been attempts to correct for some effects, e.g. [187]).

One relatively common attempt in practice to combine the various systematic errors into one term in an uncertainty calculation, is to use the MPE (see Section 5). An instrument's MPE is often mistaken for the uncertainty of measurements performed on the instrument. Whereas MPE is fundamentally limited from a GUM perspective, there have been attempts to use MPE for uncertainty evaluation in XCT ([150], [228],[242],[275]), and it is often used as one of the contributions to evaluate the uncertainty through other methods [255].

A method to achieve traceability for CMS measurements is described in ISO 15530 part 3 [144] and is specifically addressed for XCT in VDI/VDE 2630-2.1 [273]. This specification standard uses calibrated reference objects, enabling the CMS to act as a comparator. The uncertainty evaluation is based on a series of measurements on one or more calibrated objects. These measurements are executed in the same way and under the same circumstances as the workpiece measurements. This is referred to as the "substitution method". The differences between the measurement results and the calibrated values of the reference object are used for estimating the measurement uncertainty. If, e.g., an external dimension is to be measured, one can mount a calibrated length bar of similar length adjacent to the object to be measured. The latter can then be measured as a comparison. Hence, many systematic influence factors will be common to both measurements and, therefore, result in a reduced combined uncertainty after their correction. Nevertheless, similarity conditions mentioned in ISO 15530-3 are not fulfilled completely. For CMS measurements on complex parts, uncertainty evaluations are usually not performed using the substitution method since the costs and efforts for developing a suitable calibrated artefact are rapidly exceeding available means. Many groups have investigated using the substitution approach to uncertainty evaluation for XCT ([1],[24],[150],[178],[196],[201],[203],[207],[233],[274]), including for porosity measurements [118]. Some common conclusions are given below.

1. It is important to correct systematic effects, especially when it is suspected that such effects may differ for the workpiece and reference object. Examples include voxel size errors, surface determination threshold error and the effect of the surface texture.
2. There is a clear increase in evaluated measurement uncertainty when applying the substitution method to inner features (e.g. an inner as opposed to an outer diameter) and to wall thickness. This is often assumed to be due to increased effects from beam hardening and scattered radiation (although, interestingly, it has been demonstrated that beam hardening and scatter effects can sometimes mutually cancel [183]).
3. The number of repetitions that is required by ISO 15530 and VDI/VDE 2630-2.1 (minimum of twenty) is rarely adhered to due to the long measurement times for XCT instruments. There is consensus that the high degree of averaging in the XCT process means that twenty repeats is too high, and this needs to be addressed on a case-to-case basis until good practice guidance is published [201].
4. It is suggested and partially demonstrated that the experimental effort can be reduced by relying partially on simulation to establish the magnitude of some influence factors.
5. Publications differ in their interpretation of the effects of thermal drifts ([44],[100],[150]). More research is required here to establish good practice.
6. There are clear cost implications when a specific reference object is needed for every specific measurement object. These costs are associated with the production or sourcing of the reference object and its calibration.

Alternatively, a virtual measurement instrument can be used for the determination of the task-specific uncertainty of coordinate measurements. One such method is based on Monte Carlo repetition of a simulated environment and is described in ISO/TS 15530 part 4 [145]. CMS suppliers as well as third-party companies are offering uncertainty-evaluating software known as "virtual CMMs" ([20],[99]). However, such software is currently only available for contact CMS (although optical virtual CMS are under development (see [176],[281]). Virtual X-ray CMS are still under development, but early results have been published by several authors ([9],[48],[97],[114],[121],[291],[295],[296]). Measurement uncertainty is determined using a virtual CMS by repeatedly running simulations while varying influence factors on the inputs and subsequently determining how these input variations affect the measurand. The software hence estimates the variability occurring in the physical CMS measurements for each point probed. Whereas known systematic uncertainty contributions are kept constant, the random and unknown systematic contributions are varied in each simulated

measurement within their uncertainty intervals. By repeating the simulations a significant number of times it is possible to obtain a statistical evaluation of these virtual measurements, enabling a subsequent quantification of the expanded uncertainty.

The Radon transform, which gives a mathematical foundation for XCT reconstruction, models XCT as a linear model where a measurement in each pixel is given by the sum of all volume elements along a ray from source to the detector pixel. As pixel size is much larger than X-ray wavelength and in absorption-contrast attenuation dominates over other X-ray-matter interaction mechanisms, XCT acquisition can be efficiently implemented using conventional ray-tracing used in e.g. computer vision. However, this oversimplification is not sufficient to fully reproduce XCT acquisition in the virtual environment as it does not take into account polychromatic X-ray spectrum, scattering and other effects that yield a highly non-linear transfer function. Therefore these effects are either approximated numerically or measured empirically and incorporated into the measurement model.

Surface texture presents a significant issue for virtual CMS methods in terms of traceability through contact methods. The peak-to-valley deviation of the measured surface from the nominal is an important input for the uncertainty calculations. For commercial virtual CMS software packages (used with contact CMSs only), the ISO 4287 [139] *Rz* parameter can be used to define peak-to-valley deviation. Previous reviews showed that *Rz* values for metal surfaces lie between tens of nanometres to hundreds of micrometres (e.g., with an additively manufactured surface) and results show a high dependence of contact CMS measurement uncertainties on surface texture [228]. This surface texture issue is significant: it is not clear that contact CMSs can be used for traceable reference measurement without the use of a high-degree of filtering – this remains an open research question, especially with the rough surfaces encountered in additive manufacturing (AM) [174] (see Fig. 33).

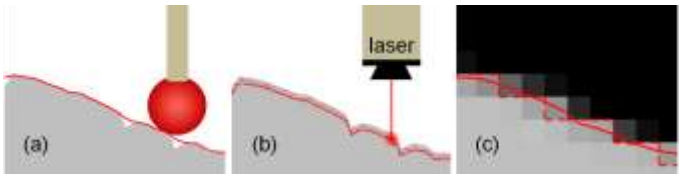

Fig. 33. Effect of surface texture on (a) contact, (b) optical and (c) XCT measurements [60].

In order to reduce excessive computational load of Monte Carlo approaches, several researchers have developed so-called "bootstrap" approaches (see Fig. 34). Bootstrapping refers to a specific type of Monte Carlo method, which evaluates properties of statistical parameters from an unknown probability distribution by repeated random drawings with replacement from the sample at hand [123]. It differs from traditional Monte Carlo approaches by not requiring prior assumptions regarding distribution functions or range of parameter values [2]. An approximated bootstrap method was developed providing straightforward uncertainty evaluation for tactile CMS measurements, and subsequently adapted to dimensional XCT [123]. In the cited examples, calibrated artefacts are used to aid the bootstrapping methods, rather than using them for task-specific uncertainty evaluation. However, the bootstrap method is primarily designed to account for random errors and cannot readily pinpoint systematic effects, so more research is required to investigate its feasibility for practical measurements. Recently, a Monte Carlo reconstruction approach was proposed that enables drastically reduced computational loads by reducing the required number of simulated projection datasets and by exploiting the concept of grey value uncertainty [97].

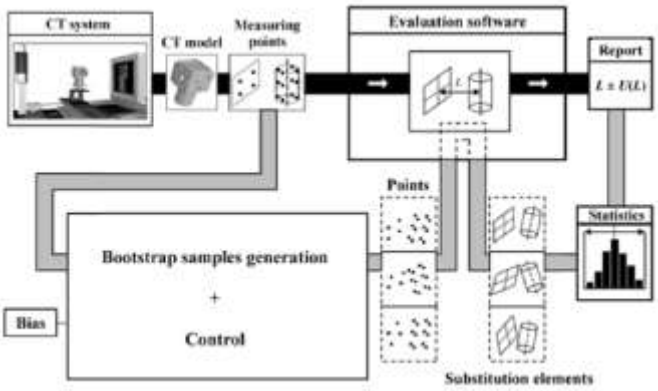

Fig. 34. Flow diagram of a typical bootstrapping process for XCT uncertainty evaluation [123].

Despite all the efforts to develop partial or whole-process measurement models for XCT, the influence of random errors and repeatability is often neglected or simply equated with noise. The measurement times associated with XCT mean that it is rare to see repeat measurements carried out, nor is it clear that simply repeating a scan can fully represent "repeatability conditions" in a classical sense. A recent review of the influence of noise on uncertainty evaluation concluded that no authors have yet proposed a complete method to estimate XCT measurement uncertainty due to noise [223]. One can observe a recent shift in how the noise contribution is being addressed. It emerges from the observation that noise does not significantly affect unidirectional measurements, such as sphere centre-to-centre distances. Moreover, no predictable trend can be observed between noise and probing errors. Therefore, research approaches are now studying the noise contribution together with other image quality parameters, such as blurring and imaging artefacts. These approaches currently seem more promising than methods that focus on an uncertainty evaluation based on merely an estimation of the noise. Some authors have hence developed techniques to evaluate image quality, mainly due to random effects ([49],[197]) and there has been recent work on how to establish confidence intervals with point cloud data in general [240], which may be applicable to XCT. Again, more research is needed to establish methods to account for random errors in XCT measurements.

The multiple measurement strategies method is currently being investigated in the EMPIR funded project EUCoM [87], but mainly for tactile CMS. The approach is based on repeated measurements of the uncalibrated workpiece placed in multiple orientations, in addition to measurements of simple length and form standards for traceability. Zanini et al. ([310],[311]) investigated the application of the multiple measurement strategies method to determine the uncertainty in the XCT measurement of an AM lattice structure. Besides testing the method on the lattice structure, Zanini et al. also compared the results of this method to those of the substitution approach, using a calibrated object developed for the purpose [310]. The authors pointed out that the main advantage of the multiple measurement strategies method compared to the substitution method is that it does not require calibrated artefacts similar to the objects that are typically measured. This advantage is potentially relevant for XCT measurements of components with complex and non-accessible geometries and surface topographies, which would be difficult or even impossible to calibrate using conventional CMSs. However, the method is not always applicable with XCT; e.g., not all objects are adequate to be measured by XCT in multiple orientations. Further research is needed to delimit the conditions in which method is actually applicable to ensure reliable uncertainty determination and correction of systematic errors.

7. Performance in various applications and interlaboratory comparisons

The application of industrial XCT continues to grow, spanning from defect analysis and material characterization to reverse engineering and dimensional metrology (Fig. 35). Various examples of industrial applications are provided elsewhere ([52],[73]). This section presents a brief review of XCT performance for various applications. First an overview of interlaboratory comparisons targeting dimensional and geometrical feature measurements is given. Subsequently, recent insights into the performance for surface topography, porosity measurements, and particle and fibre measurements are presented.

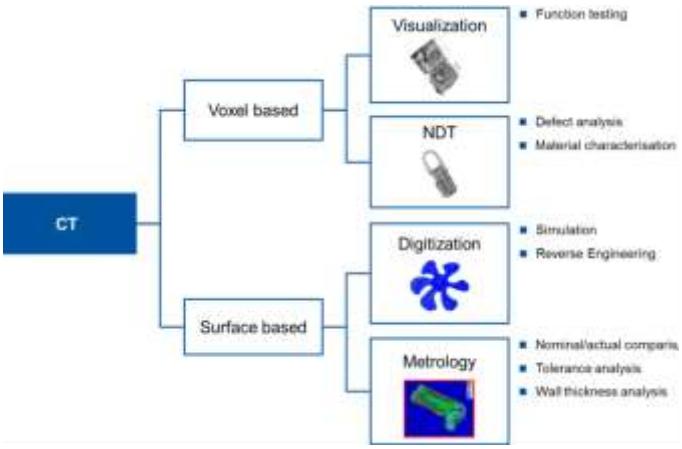

Fig. 35. Industrial applications of XCT [52].

7.1 Interlaboratory comparisons for dimensional and geometrical feature metrology

The results from the first international comparison of XCT instruments used for dimensional metrology ("CT Audit") were published in 2012 [61], involving fifteen instruments. Four calibrated reference objects were measured, with different dimensions, geometries and materials. This first comparison showed that, whilst most of the size measurements were performed with sub-voxel accuracy, form measurements were less accurate and, in more than half of the cases, the participants were not able to supply valid uncertainty statements or significantly overestimated the uncertainty. This early publication highlighted the need for traceability and standardisation; almost ten years on, research is still needed despite the progress made since then. Following CT Audit, a further comparison of dimensional measurements using XCT was published in 2014 [14], involving twenty-seven participants and the use of polymer and metal components ("CIA-CT"). The results were similar to those from CT Audit, with quoted expanded uncertainties ranging from 1 µm to 50 µm, again highlighting the need for traceability and standardisation.

As part of the EU-funded InteraqCT project, a comparison of twenty laboratories was conducted using physical (step gauge in a tube, calibrated using contact CMM) and virtual (data sets) assemblies [257]. Relatively good agreement between the reference and participants' results was obtained and 90 % of the participants quoted measurement uncertainties (using a range of protocols). It was found that several participants were overestimating uncertainty but that they could significantly decrease their measurement times, with minimal effect on uncertainty. It was noted that the definition of datums is a significant issue for XCT measurements. Fig. 36 summarises the results from CT-Audit, CIA-CT and InteraqCT comparisons, and illustrates the range of the quoted uncertainties – still much larger in range and value compared to that for contact CMMs [276].

A comparison was conducted of industrial and medical XCT systems, with the premise that, when low resolutions can be tolerated, medical CT systems can be much faster (in terms of both scanning time and subsequent data analysis) and able to measure large objects [82]. This preliminary study showed some interesting results, but the limited availability of medical systems at industrial sites means that the concept is not being widely adopted in industry.

With the increasing interest in measuring additively manufactured components, there have been some recent XCT comparisons involving AM components [84]. One comparison involves the measurement of a 10 mm cube, a 15 mm diameter cylindrical rod and a 40 mm by 60 mm complex bracket; all parts were metal. The parts were designed to compare the capabilities of the twelve participants to measure defect types, such as surface and bulk pores. Significant differences were found in the quantitative evaluations made by the participants, ranging from no quantitative measurements performed, to under and overestimation of the dimensional results. The comparison highlighted typical imaging artefacts and, again, the need for standards for measurement protocols and analysis pipelines. Another comparison concerning XCT for AM components was carried out under the European project AdvanCT. Reference standards featuring internal and external inserts in three materials (ABS, aluminium, and stainless steel), covering measurands from 0.25 mm up to 28.5 mm, were circulated among 10 European laboratories [204]. The results show that the participants have reported XCT measurements in good agreement with the reference CMM measurements [205].

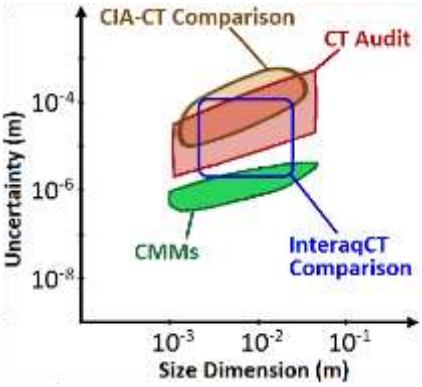

Fig. 36. Situating different CT interlaboratory intercomparisons [276].

7.2 Surface topography measurements

Tomographic reconstruction consists of resolving the three-dimensional photon attenuation map of a scanned object from the collection of projection measurement. The attenuation map is typically discretised onto regular 3D grid, i.e. voxel volume. Sharp change in attenuation corresponds either to interface between two materials with different X-ray attenuation properties or to the transition from background (air) to material. As surface determination allows to extract a surface corresponding to a specific part, XCT can be used to reconstruct the part surfaces and, if the resolution permits, surface texture (e.g. [219],[264],[268]).

XCT is capable of capturing re-entrant surfaces, and even internal pores/cavities that would be otherwise inaccessible to other measurement technologies. XCT is the only method which gives access to deep recesses and otherwise difficult to reach surfaces of an AM component. This not only applies to generally planar AM surfaces that are challenging to measure because of high aspect ratio features (adhering powder particles, deep recesses,

etc.), but also to the surfaces of AM parts of complex geometry (lattice structures, hollow parts, etc.) which would not be accessible with any other measurement method ([73],[83],[265],[266],[268],[307]). An example topography of a laser-based powder bed fusion (L-PBF) surface measured by XCT is given in Fig. 37. Because of the fully 3D nature of the topography captured by the method, triangle mesh representations are required to store the measurement result and conversion to a height map is required before texture parameters can be computed. Recently research into computation of areal surface texture parameters on triangular meshed surfaces directly, avoids the need to convert from areal map to 3D mesh [209].

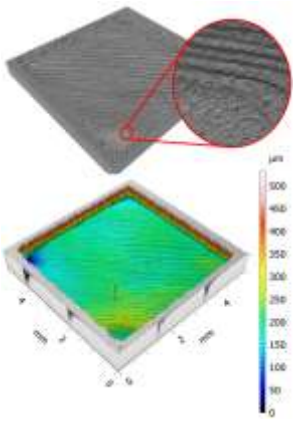

Fig. 37. AM surface texture as measured by XCT.

Surface determination errors are relevant in dimensional metrology, and even more so when the interest is in the analysis of geometric formations existing at smaller scales (e.g., surface topography) that are comparable with the minimum observational scales currently possible with XCT measurement of dense metals ([182],[306]). Other sources of error include voxel and focal spot size variations and beam hardening effects. There has been some recent work to develop methods for uncertainty evaluation for surface measurements with XCT. Zanini et al. [308] used a sample cross-section and obtained traceability through a vision CMS, although the uncertainty would be highly dominated by the calibration influence factor. Rodríguez-Sánchez et al. [224] are attempting to apply the ISO 25178-600 [147] metrological characteristic framework (see Leach et al. for a recent overview [175]) to XCT and are developing a dedicated artefact, shown in Fig. 38.

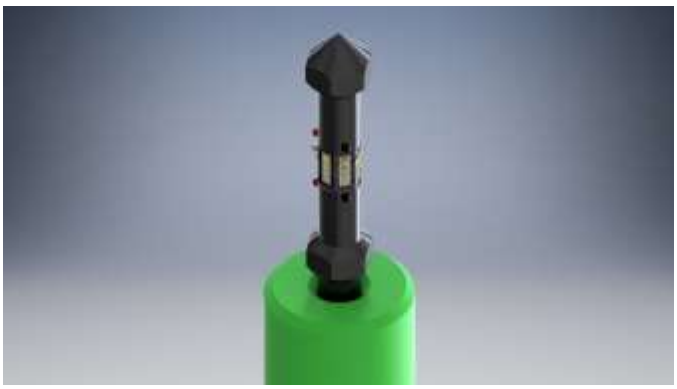

Fig. 38. Artefact, comprising multiple ISO 25178-70 material measures, for the calibration of surface texture measurements using XCT [146].

Surface topography measurement using XCT has come a long way in the last five years and will continue to be an important measurement technology as internal surfaces need to be accessed. Today the measurement uncertainty can already be evaluated using ISO methods, although, as with all measurement technologies, there is still some research required to develop methods for evaluating the contribution to uncertainty due to topographic fidelity [175].

7.3 Porosity measurements

An important application of industrial XCT is the study of the occurrence of porosity during manufacturing processes such as casting, welding or additive manufacturing [315]. Dimensional measurement challenges include locating the position of the pores, examining size distribution of pores and understanding the diversity in pore shape (spherical gas entrapment or “keyhole” pores, elongated sharply edged “lack of fusion” pores, etc.). Some algorithms are developed within research institutions, though some popular commercial algorithms are also commonplace (e.g., in VGStudioMAX 3.5 [284] commercial software).

There have been many studies of porosity measurement recently, using a variety of detection algorithms. For example, Zhu et al. [315] used XCT to investigate the evolution of pore generation during subsequent steps of a binder jetting AM process, and revealed that reticulated pores in the green state break up during sintering, and subsequently evolve into smaller quasi-spherical pores during hot isostatic pressing. Pavan et al. [211] used XCT to study the occurrence of interlayer pores in the polymer powder bed fusion process, noting that an increase in X-ray power negatively influenced the porosity measured, likely due to the increase in the size of the source focal spot, and that algorithmic noise reduction tended to modify the size of the measured pores. So increasing the number of projections was preferred as a method of noise reduction. However, repeatability over various reconstructions of a single input dataset was high. Similarly, du Plessis et al. demonstrated an approach to porosity analysis using XCT, examining methods of porosity analysis on 2D slice images as well as 3D volumetric reconstructions [81]. These authors found that both forms of analysis were useful for investigating different aspects of part porosity, with 2D analysis providing indications of the porosity variation within an object and 3D analysis providing pore size distribution, visual inspection of particular pores and pore categorisation. Xu et al. [300] examined the evolution of porosity in an additively manufactured part using XCT during a staged thermomechanical test, pausing the test at regular intervals to track the changes in pore shape and size during the test. By retrospectively examining the data, the authors were able to identify a pore that ultimately caused part failure and track its progression through the test.

Efforts have been made to establish traceability in porosity measurements, such as in the work performed by Heřmánek et al. [119]. While traceability was established in this case, the authors note that, to do so, a traceable reference measurement must be made of a similar sample and this information used in the adjustment of the surface determination algorithm (i.e. the substitution method of uncertainty evaluation, see Section 6). While the substitution method is viable in many scenarios, it requires reference measurements to be made on a reference object that is similar in composition, shape, and size to the test object and such an uncertainty evaluation cannot easily be generalized to dissimilar workpieces. As such, as far as the authors of this paper are aware of, a method for traceable measurement of pores independent from the object material has not yet been demonstrated in the literature.

Recent studies into XCT porosity measurement have further developed the available technology, through the application of machine learning to porosity detection (e.g. [34],[105]). The authors of such studies used machine learning to automatically segment pores from the surrounding material, though noted issues relating to the impact of imaging artefacts and noise on the machine learning algorithm’s performance. In these studies,

neural network parameter optimisation and the range of segmentation methodologies were used to train the machine learning algorithm; however, traceability was not discussed in reference to porosity measurement. Similarly, Lifton and Liu [186] recently presented a locally adaptive method for segmentation of pores from background material, developed to address the influence of beam hardening artefacts that occur during the measurement of particularly radiopaque parts. The authors compared results from their algorithm to reference measurements made using the Archimedes principle, finding more accurate results compared to the current state of the art in pore detection algorithms, but noting continuing challenges relating to limited voxel resolution, multi-material parts, computational expense and the influence of different XCT scan settings. Lifton and Liu also discuss difficulties in establishing traceability for AM porosity measurements in reference to the work performed by Heřmánek et al. [119], particularly noting that "the machined hemispherical features of the reference object used [in Heřmánek et al.'s work] to represent internal pores cannot be considered to be representative of the variety of pore shapes and sizes encountered in AM parts, nor is a single part geometry representative of the wide variety of part geometries achievable using AM". Comparison of XCT with other methods is therefore essential to validate the capability of XCT to measure the actual characteristics of pores. Several works investigated the ability of XCT on detecting small pores, in relation to the voxel size and compared to other methods such as Archimedes and ultrasonic testing (e.g., see [117],[294]).

In addition to the difficulties faced in establishing measurement traceability, there remains a difficulty in XCT porosity measurement with understanding the algorithms used to identify pores – academic studies (see, e.g. Xu et al. [300]) commonly explain detection methods in detail but are relatively rudimentary in their approaches, while commercial algorithms (e.g., the algorithm employed in VGStudioMAX 3.5 [284]) claim notably more advanced detection paradigms, but the specific methodologies employed by those algorithms (understandably) remain shrouded behind the veil of commercial secrecy. Such secrecy is essential for the success of the companies supplying these algorithms but presents an additional barrier in understanding how to detect porosity in a repeatable and reliable manner. The focus of ongoing work tends to be on iterating new methods of pore detection (e.g., see [105]) or, more commonly, to apply existing pore detection methods to novel scenarios (e.g., see [78],[79]). Beyond the work performed by Heřmánek et al. [119], there have been no further efforts to establish traceability in porosity measurement, and this problem remains a significant challenge to address in future porosity measurement research.

7.4 Fibre and particle measurements

Another relevant application of industrial XCT is fibre analysis for composite materials and particularly for fibre-reinforced polymers (FRPs). Several methods have been developed for measuring the geometrical characteristics of fibres reconstructed from XCT data ([63],[102]). In particular, the characteristics of interest are those having a direct influence on mechanical properties and the performance of FRP, including fibre orientation, length and volume fraction [289]. Recent research has focused on the traceability of XCT measurements of fibre characteristics, applying the substitution method and using reference objects with calibrated fibres ([189],[309]).

Particle size distributions have been assessed using XCT [246] in view of, e.g., developing a better understanding of the influence of powder characteristics on the eventual properties of powder bed fusion AM workpieces [247]. It has been shown that XCT based characterization of powder using principal component analysis outperforms conventional 2D data-based methods for particle analysis, whereby the latter overestimated particle mass by a factor of 2.3 [225].

8. Conclusions and research needs

Over the last decades, industrial XCT has seen a strong expansion of its capabilities and applications, due to a continuous improvement in its performance, resulting from a combination of improved X-ray sources, detectors, algorithms, computing capabilities, and sound metrological practice. There is little reason to believe that this progress will stall. For example, many advanced solutions for enhanced X-ray sources are now available and continue to be developed, allowing for increased attainable X-ray fluxes at small focal spot sizes, therefore, bridging the gap between tube and synchrotron sources, and enabling faster yet higher-resolution tomography. Similarly, new imaging methods continue to emerge and advance, such as multi-energy XCT. New detectors are and will continue to offer possibilities that were not available or too expensive a few years ago, including photon-counting detectors that enable material decomposition and spectral XCT.

Computational performance will enable further developments regarding iterative reconstruction as well as various XCT artefact corrections (see Section 4.3). Major challenges are related to the unsolved trade-off between speed and quality, since high-quality scans are excessively time consuming regarding both set-up times and actual scanning times. Important developments are, therefore, to be expected regarding XCT based on a reduced expert user input (see Section 2.3) as well as faster XCT acquisition, while maintaining or even improving image quality and ensuring traceability.

In order to achieve traceability of XCT, it is essential to further increase the understanding of how the X-ray physics and deviations from the ideal conditions propagate through the complex data processing pipeline [124]. Artefact correction (e.g. scatter, beam hardening, etc.) that is based on such an understanding will remain a subject of further study and developments for the foreseeable future with special emphasis on the performance of multi-material scans. Advanced artefact correction algorithms are essential to reduce systematic and random errors, but also contribute to an increased complexity of the data processing chain and, thus, to additional challenges for traceable metrology. One observes, e.g., that XCT will also in future be steered increasingly by deep learning-based data processing algorithms. Despite their popularity in many engineering disciplines, their lack of capability to estimate prediction uncertainty nevertheless causes issues in their implementation for measurement applications: they are effectively "black-box" systems, or ever-changing shades of grey. A further challenge with the established methods to evaluate uncertainty is that error propagation is based on the availability of supporting, deterministic models that describe how information propagates through the various stages of data processing and analysis [286]. The introduction of machine learning methods raises currently unanswered questions related to how such support models may be adapted to accommodate machine learning data processing steps [66]. Whilst machine learning may be "just another model" and error propagation may be trivial, there has been little research to date to investigate this [30].

Moreover, the use of non-standard trajectories, such as limited angle and robot-based XCT are expected to gain importance. Additional research will be required to fully exploit the potential of XCT as an integral part of the manufacturing intelligence loop. In the context of decreasing lot sizes, traditional methods of quality inspection are becoming inadequate. Thus, big data collected by fully in-line XCT systems needs to be coupled to the manufacturing process planning, simulation, and machine learning in order to exploit its full potential, to increase the understanding of key

manufacturing processes, and to allow first-time-right manufacturing.

Faster acquisition will benefit from the use of multiple X-ray tubes to collect many projections in rapid succession, which may enable XCT as an in-line measurement tool for several manufacturing processes. Such developments will need to be accompanied by dedicated, fast methods for traceability establishment, including tailored procedures and calibrated objects for error characterisation and metrological performance verification. Fast XCT is being used in some fields of research for time-lapse and 4D imaging (3D + time). When sufficiently fast metrological solutions will be available in addition to the large computing power required for analysing 4D data, 4D imaging can become a real possibility for XCT manufacturing metrology.

Acknowledgements

The authors extend thank to Dr. Evelina Ametova (Karlsruhe Institute of Technology), Prof. Andreas Archenti (KTH), Prof. Leonardo De Chiffre (DTU), Dr. Alkan Donmez (NIST), Dr. Massimiliano Ferrucci (LLNL), Prof. Jean-Pierre Kruth (KU Leuven), Dr Ulrich Neuschaefer-Rube (PTB), Dr Adam Thompson (Univ. of Nottingham), Dr. Filippo Zanini (Univ. Padova) for their valuable contributions and comments. We are moreover grateful to the colleagues of CIRP STC-P who have contributed to the quality of this paper through valuable discussions, comments and feedback. For the financial support thanks are devoted to the many organizations that have funded research on CT metrology in the labs of the authors, including the FWO MetroFlex project (S004217N).

References

[1] Affenzeller C, Gusenbauer C, Reiter M, Kastner J (2015). Measurement uncertainty evaluation of an X-ray computed tomography system. Proc. Digital Industrial Radiology and Computed Tomography, Ghent, 22-25 June.

[2] Aggogeri F, Barbato G, Barini EM, Genta G, Levi R (2011). Measurement uncertainty assessment of coordinate measuring machines by simulation and planned experimentation. CIRP Journal of Manufacturing Science and Technology 4:51-56.

[3] Aloisi V, Carmignato S (2016). Influence of surface roughness on X-ray computed tomography dimensional measurements of additive manufactured parts. Case studies in nondestructive testing and evaluation, 6, 104-110.

[4] Aloisi V, Carmignato S, Schlecht J, Ferley E (2016). Investigation on metrological performances in CT helical scanning for dimensional quality control. Proc. iCT2016 Conference on Industrial Computed Tomography, Wels, 9-12 February.

[5] Aloisi V, Schlecht J, Ferley E, Carmignato S (2019). Characterization of the effects of detector angular misalignments and accuracy enhancement of X-ray CT dimensional measurements. Proc. iCT2019 Conference on Industrial Computed Tomography, Padova, 13-15 February.

[6] Alvarez RE, Macovski A (1976). Energy-selective reconstructions in x-ray computerised tomography. Physics in Medicine & Biology, 21(5), 733.

[7] Ametova E, Ferrucci M, Dewulf W (2017). A tool for reducing cone-beam artifacts in computed tomography data, Proc. iCT2017 Conference on Industrial Computed Tomography, Leuven, 7-9 February.

[8] Ametova E, Ferrucci M, Chilingaryan S, Dewulf W (2018). Software-based compensation of instrument misalignments for x-ray computed tomography dimensional metrology. Precision Engineering, 54, 233-242.

[9] Ametova E, Ferrucci M, Chilingaryan S, Dewulf W (2018). A computationally inexpensive model for estimating dimensional measurement uncertainty due to x-ray computed tomography instrument misalignments. Meas. Sci. Technol. 29 065007.

[10] Ametova E (2019). Quantification and compensation of geometry-induced errors in cone-beam X-ray computed tomography. PhD Dissertation, KU Leuven.

[11] Amirkhanov C, Heinzl M, Reiter J, Kastner M, Gröller E (2011). Projection-based metalartifact reduction for industrial 3D X-ray computed tomography. IEEE Trans. Vis. Comput. Graph. 17(12), 2193–2202.

[12] Anas EMA, Kim JG, Lee SY, Hasan MK (2011). Comparison of ring artifact removal methods using flat panel detector based CT images. Biomedical engineering online, 10(1), 1-25.

[13] Angel J, De Chiffre L (2013). Inter laboratory comparison on Industrial Computed Tomography. CIA-CT comparison. Final Report. DTU, Lyngby.

[14] Angel J, De Chiffre L (2014). Comparison on Computed Tomography using industrial items. CIRP Annals, 63(1), 473-476.

[15] Arenhart FA, Nardelli VC, Donatelli GD (2015). Characterization of the metrological structural resolution of CT systems using a multi-wave standard. Proc. XXI IMEKO World Congress, Prague, 30 August – 4 September, p. 1340-1345.

[16] Arenhart FA, Baldo CR, Fernandes TL, Donatelli GD (2016). Experimental Investigation of the Influencing Factors on the Structural Resolution for Dimensional Measurements with CT Systems. Proc. iCT2016 Conference on Industrial Computed Tomography, Wels, 9-12 February.

[17] ASTM E1165-12 (2017). Standard Test Method for Measurement of Focal Spots of Industrial X-Ray Tubes by Pinhole Imaging.

[18] Baier M et al. (2018). A new conversion approach between different characterization methods to measure the spot size of micro computed tomography systems. Proc. 18th euspen conference, Venice, Italy, 4-8 June, p. 445-446.

[19] Baier M (2021). Enhancing the precision of metal additive manufacturing through advanced metrological X-ray computed tomography. PhD thesis, University of Padova.

[20] Balsamo A, Di Ciommo M, Mugno R, Rebaglia BI, Ricci E, Grella R (1999). Evaluation of CMM uncertainty through Monte Carlo simulations. Annals CIRP 48:425–428.

[21] Bartscher M, Hilpert U, Härtig F, Neuschaefer-Rube U, Goebbels J, Staude A (2008) Industrial computed tomography, an emerging coordinate measurement technology with high potentials, Proc. NCSL 2008 International workshop & symposium, 3-7 August, ISBN 1-584-64058-8

[22] Barna SL, Tate MW, Gruner SM, Eikenberry EF (1999). Calibration procedures for charge-coupled device x-ray detectors. Rev Sci Instrum 70(7):2927–2934.

[23] Barrett JF, Keat N (2004). Artifacts in CT: Recognition and Avoidance. Radiographics, 24:1679–1691. DOI: 10.1148/rg.246045065

[24] Bartscher M, Neukamm M, Hilpert U, Neuschaefer-Rube U, Härtig F, Kniel K, Ehrig K, Staude A, Goebbels J (2010). Achieving traceability of industrial computed tomography. Key Engineering Materials 437:79-83.

[25] Bartscher M, Neukamm M, Koch M, Neuschaefer-Rube U, Staude A, Goebbels J, Ehrig K, Kuhn C, Deffner A, Knoch A (2010). Performance assessment of geometry measurements with micro-CT using a dismountable work-piece-near reference standard. Proc. 10th European Conference on Non-Destructive testing, Moscow, 7-11 June.

[26] Bartscher M, Staude A, Ehrig K, Ramsey A (2012). The influence of data filtering on dimensional measurements with CT. Proc. World conf. of Nondestructive testing, Durban; 16-20 April.

[27] Bartscher M, Sato O, Härtig F, Neuschaefer-Rube U (2014). Current state of standardization in the field of dimensional computed tomography. Measurement Science and Technology, 25(6), 064013.

[28] Bartscher M, Illemann J, Neuschaefer-Rube U (2016). ISO test survey on material influence in dimensional computed tomography. Case studies in nondestructive testing and evaluation, 6, 79-92.

[29] Bartscher M, Neuschaefer-Rube U, Illemann J, de Oliveira FB, Stolfi A, Carmignato S (2018). Qualification and testing of CT systems. In: Carmignato S, Dewulf W, Leach RK. Industrial x-ray computed tomography. Springer.

[30] Basu T, Einbeck J, Troaes MCM, Forbes A (2019). Robust uncertainty quantification for measurement problems with limited information ISIPTA 2019 Ghent, 3-6 July.

[31] Batenburg KJ, Sijbers J (2011). DART: A Practical Reconstruction Algorithm for Discrete Tomography. IEEE Trans Image Process 2011;20:2542–53.

[32] Batenburg KJ, Palenstijn WJ, Balázs P, Sijbers J (2013). Dynamic angle selection in binary tomography. Computer Vision and Image Understanding, 117(4), 306-318.

[33] Beister M, Kolditz D, Kalender WA (2012). Iterative reconstruction methods in X-ray CT. Physica medica, 28(2), 94-108.

[34] Bellens S, Vandewalle P, Dewulf W (2021). Deep learning based porosity segmentation in X-ray CT measurements of polymer additive manufacturing parts. Procedia CIRP, 96, 336-341.

[35] Beucher S (1979). Use of watersheds in contour detection. In Proceedings of the International Workshop on Image Processing. CCETT, p. 17-21.

[36] Bieberle M, Fischer F, Schleicher E, Hampel U, Koch D, Aktay KDC, Menz HJ, Mayer HG (2007). Ultrafast limited-angle-type x-ray tomography. Applied Physics Letters, 91(12), 123516.

[37] Bircher BA, Meli F, Küng A, Thalmann R (2017). Towards metrological computed tomography at METAS. Euspen's 17th International Conference & Exhibition, Hannover, 29 May – 2 June.

[38] Bircher BA, Meli F, Küng A, Thalmann R (2018). A geometry measurement system for a dimensional cone-beam CT. Proc. iCT2018 Conference on Industrial Computed Tomography, Wels, 6-9 February.

[39] Bircher BA, Meli F, Küng A and Thalmann R (2019). CT geometry determination using individual radiographs of calibrated multi-sphere standards. Proc. iCT2019 Conference on Industrial Computed Tomography, Padova, 13-15 February.

[40] Bircher BA, Meli F, Küng A, Thalmann R (2019). CT machine geometry changes under thermal load. Proc. iCT2019 Conference on Industrial Computed Tomography, Padova, 13-15 February.

[41] Bircher BA, Meli F, Küng A, Thalmann R (2020). METAS-CT: Metrological X-ray computed tomography at sub-micrometre precision. Proc. the 20th euspen international conference, 8-12 June, pp. 281–284.

[42] Boas FE, Fleischmann D (2012). CT artifacts: causes and reduction techniques. Imaging Med. 4, 229–240.

[43] Boeckmans B, Tan Y, Welkenhuyzen F, Guo Y, Dewulf W, Kruth JP (2015). Roughness offset differences between contact and non-contact measurements.

In Proceedings of the 15th international conference of the European society for precision engineering and nanotechnology, 1-5 June, pp. 189-190.
[44] Borges De Oliveira F, de Campos Porath M, Nardelli VC, Arenhart FA, Donatelli GD (2014). Characterization and correction of geometric errors induced by thermal drift in CT measurements. Key Engineering Materials, Vol. 613, pp. 327-334.
[45] Borges de Oliveira FB, Bartscher M, Neuschaefer-Rube U (2015). Analysis of combined probing measurement error and length measurement error test for acceptance testing in dimensional computed tomography. Proc. Digital Industrial Radiology and Computed Tomography, Ghent, 22-25 June.
[46] Borges de Oliveira F, Stolfi A, Bartscher M, De Chiffre L, Neuschaefer-Rube U (2016). Experimental investigation of surface determination process on multi-material components for dimensional computed tomography. Case Stud. Nondestruct. Test. Eval., Vol. 6B, pp.93-103.
[47] Bouhaouel F, Bauer F, Grosse CU (2020). Task-specific acquisition trajectories optimized using observer models. Proc. iCT2020 Conference on Industrial Computed Tomography, Wels, 4-7 February.
[48] Bredemann J, Schmitt RH (2018). Task-specific uncertainty estimation for medical CT measurements. Journal of Sensors and Sensor Systems, 7:627-635.
[49] Brierley N, Nye B, McGuinness J (2019). Mapping the spatial performance variability of an X-ray computed tomography inspection. NDT & E International, 107:102127.
[50] Brooks RA, Di Chiro G (1976). Beam hardening in x-ray reconstructive tomography. Physics in medicine & biology, 21(3), 390.
[51] Buratti A, Ben Achour S, Isenberg C, Schmitt R (2016). Frequency-based method to optimize the number of projections for industrial computed tomography. Proc. iCT2016 Conference on Industrial Computed Tomography, Wels, 9-12 February.
[52] Buratti A, Bredemann J, Pavan M, Schmitt R, Carmignato S (2018). Applications of CT for Dimensional Metrology. In Carmignato S., Dewulf W, Leach RK, Industrial X-ray Computed Tomography, Springer.
[53] Busch M, Hausotte T (2021) Determination of the Interface Structural Resolution of an Industrial X-Ray Computed Tomograph Using a Spherical Specimen and a Gap Specimen, Consisting of Gauge Blocks. Key Engineering Materials, Vol. 883, pp. 41-48.
[54] Buzug TM (2008) Computed tomography: from photon statistics to modern cone-beam CT. Springer.
[55] Cantatore A, Andreasen JL, Carmignato S, Müller P, De Chiffre L (2011) Verification of a CT scanner using a miniature step gauge. Proc. 11th euspen conference, Como, 23-26 May, pp. 46–49.
[56] Cao W, Sun T, Kerckhofs G, Fardell G, Price B, Dewulf W (2018). A simulation-based study on the influence of the x-ray spectrum on the performance of multi-material beam hardening correction algorithms. Measurement Science and Technology, 29(9), 095002.
[57] Cao W (2019). Development of Beam Hardening Correction Algorithms for Industrial Computed Tomography. PhD Dissertation, KU Leuven.
[58] Cao W, Pauwels R, Fardell G, Price B, Dewulf W (2019). Influencing factors in x-ray spectral estimation of industrial CT using transmission measurements. Proc. iCT2019 Conference on Industrial Computed Tomography, Padova, 13-15 February.
[59] Canny J (1986). A computational approach to edge detection. IEEE Transactions on pattern analysis and machine intelligence, (6), 679-698.
[60] Carmignato S, Savio E (2011) Traceable Volume Measurements Using Coordinate Measuring Systems. CIRP Annals, 60:519-522.
[61] Carmignato S (2012). Accuracy of industrial computed tomography measurements: Experimental results from an international comparison. CIRP Annals, 61:491-494.
[62] Carmignato S, Aloisi V, Medeossi F, Zanini F, Savio E (2017). Influence of surface roughness on computed tomography dimensional measurements. CIRP Annals, 66(1), 499-502.
[63] Carmignato S, Dewulf W, Leach R (2018) Industrial X-ray Computed Tomography. Springer.
[64] Carmignato S, De Chiffre L, Bosse H, Leach RK, Balsamo A, Estler WT (2020). Dimensional artefacts to achieve metrological traceability in advanced manufacturing. CIRP Annals, 69(2):693–716.
[65] Chase, R. C., & Stein, J. A. (1978). An improved image algorithm for CT scanners. Medical physics, 5(6), 497-499.
[66] Cheung H, Braun JE (2016). A general method for calculating the uncertainty of virtual sensors for packaged air conditioners Int. J. Refrig. 63 225-236.
[67] Christoph R, Neumann HJ (2011) X-ray Tomography in Industrial Metrology: Precise, Economical and Universal. Verlag moderne industrie.
[68] Cierniak R (2011) X-Ray computed tomography in biomedical engineering. Springer.
[69] CIRP (2019) CIRP Encyclopedia of Production Engineering. Springer.
[70] Cuadra J, Divin C, Panas R (2017). Uncertainty quantification of an X-ray computed tomography system. Euspen special interest group meeting: additive manufacturing, Leuven, 10-11 October.
[71] Dabravolski, A., Batenburg, K. J., & Sijbers, J. (2014). Dynamic angle selection in x-ray computed tomography. Nuclear Instruments and Methods in Physics Research Section B: Beam Interactions with Materials and Atoms, 324, 17-24.
[72] Davis GR, Elliott JC (1997). X-ray microtomography scanner using time-delay integration for elimination of ring artefacts in the reconstructed image. Nucl Instrum Methods Phys Res Sect A 394(1-2), 157–162.
[73] De Chiffre L, Carmignato S, Kruth JP, Schmitt R, Weckenmann A (2014). Industrial applications of computed tomography. CIRP Annals - Manufacturing Technology, 63, 655–677.
[74] Dewulf W, Tan Y, Kiekens K (2012). Sense and non-sense of beam hardening correction in CT metrology. CIRP annals, 61(1), 495-498.
[75] Dewulf W, Kiekens K, Tan Y, Welkenhuyzen F, Kruth JP (2013). Uncertainty determination and quantification for dimensional measurements with industrial computed tomography. CIRP Annals 62:535-538.
[76] Dewulf W, Ferrucci M, Ametova E, Heřmánek P, Probst G, Boeckmans B, Craeghs T, Carmignato S (2018). Enhanced Dimensional Measurement by Fast Determination and Compensation of Geometrical Misalignments of X-Ray Computed Tomography Instruments. CIRP Annals, 67:1, 523-526.
[77] Di Domenico G, Cardarelli P, Contillo A, Taibi A, Gambaccini M (2016). X-ray focal spot reconstruction by circular penumbra analysis-Application to digital radiography systems. Med. Phys. 43 (1), 294-302.
[78] Dilonardo E, Nacucchi M, De Pascalis F, Zarrelli M, Giannini C (2020). High resolution X-ray computed tomography: a versatile non-destructive tool to characterize CFRP-based aircraft composite elements. Compos. Sci. Technol. 192:108093.
[79] Dionnet Z, Suttle MD, Longobardo A, Rotundi A, Folco L, Della Corte V, King A (2020). X-ray computed tomography: morphological and porosity characterization of giant Antarctic micrometeorites. Meteorit. Planet. Sci. 55:1581–1599.
[80] Do TD, Sawall S, Heinze S, Reiner T, Ziener CH, Stiller W, Schlemmer HP, Kachelrieß M, Kauczor HU, Skornitzke S (2020). A semi-automated quantitative comparison of metal artifact reduction in photon-counting computed tomography by energy-selective thresholding. Scientific Reports, 10(1), 1-10.
[81] du Plessis A, Olawuyi BJ, Boshoff WP, le Roux SG (2016). Simple and fast porosity analysis of concrete using X-ray computed tomography. Mater. Struct. Constr. 49:553–562.
[82] du Plessis A, le Roux SG, Guelpa A (2016). Comparison of medical and industrial X-ray computed tomography for non-destructive testing. Case Studies Nondestruc. Test. Eval. 6:17-25.
[83] du Plessis A, Yadroitsev I, Yadroitsava I, Le Roux SG (2018). X-ray microcomputed tomography in additive manufacturing: A review of the current technology and applications. 3D Print. Addit. Manuf. 5:227-247.
[84] du Plessis A, le Roux SG, Waller J, Sperling P, Achilles N, Beerlink A, Métayer JF, Sinico M, Probst G, Dewulf W, Bittner F, Endres HJ, Willner M, Drégelyi-Kiss Á, Zikmund T, Laznovsky J, Kaiser J, Pinter P, Dietrich S, Lopez E, Fitzek O, Konrad P (2019). Laboratory X-ray tomography for metal additive manufacturing: Round robin test. Additive Manufacturing, 30:100837.
[85] du Plessis A, Tshibalanganda M, le Roux SG (2020). Not all scans are equal: X-ray tomography image quality evaluation. Materials Today Communications, 22, 100792.
[86] EN 12543-5 (1999). Characteristics of Focal Spots in Industrial X-ray Systems for Use in Non-destructive Testing—Part 5: Measurement of the Effective Focal Spot Size of Mini and Micro Focus X-ray Tubes.
[87] EUCoM project website. http://eucom-empir.eu/. Visited 10 April 2022.
[88] Eulig E, Maier J, Bennett NR, Knaup M., Hörndler K, Wang A, Kachelrieß M (2020). Deep learning-aided CBCT image reconstruction of interventional material from four x-ray projections. Medical Imaging 2020: Physics of Medical Imaging, Vol. 11312, p. 113121L. International Society for Optics and Photonics.
[89] Feldkamp LA, Davis J, Kress JW (1984) Practical cone-beam algorithm. J. Opt. Soc. Amer. 1 A6 (612-619).
[90] Ferrucci M, Leach RK, Giusca C, Carmignato S, Dewulf W (2015). Towards geometrical calibration of x-ray computed tomography systems—a review. Measurement Science and Technology, 26(9), 092003.
[91] Ferrucci M, Ametova E, Carmignato S, Dewulf W (2016). Evaluating the effects of detector angular misalignments on simulated computed tomography data. Precis Eng, 45, 230-241.
[92] Ferrucci M, Heřmánek P, Ametova E, Carmignato S, Dewulf W (2018). Measurement of the X-ray computed tomography instrument geometry by minimization of reprojection errors—Implementation on simulated data. Precision Engineering, 54, 7-20.
[93] Ferrucci M, Heřmánek P, Ametova E, Sbettega E, Vopalensky M, Kumpová I, Vavřík D, Carmignato S, Craeghs T, Dewulf W (2018). Measurement of the X-ray computed tomography instrument geometry by minimization of reprojection errors—Implementation on experimental data. Precision Engineering, 54, 107-117.
[94] Ferrucci M (2018). Systematic approach to geometrical calibration of X-ray computed tomography instruments. PhD dissertation, KU Leuven.
[95] Ferrucci M, Ametova E (2021). Charting the course towards dimensional measurement traceability by X-ray computed tomography. Measurement Science and Technology. **32:**092001
[96] Ferrucci M, Dewulf W, Dönmez A (2021). Measurement of sample stage error motions in cone-beam X-ray computed tomography instruments by minimization of reprojection errors. Precision Engineering, 67, 48-57.
[97] Ferrucci M, Ametova E, Dewulf W (2021). Monte Carlo reconstruction: a concept for propagating uncertainty in computed tomography. Meas. Sci. Technol. 32 115006 .
[98] Fischer A, Lasser T, Schrapp M, Stephan J, Noël PB (2016). Object specific trajectory optimization for industrial x-ray computed tomography. Scientific reports, 6(1), 1-9.
[99] Flack DR (2013). Co-ordinate measuring machines task specific measurement uncertainties. NPL Good Practice Guide No. 130, National Physical Laboratory.

[100] Flay N, Sun W, Brown S, Leach RK, Blumensath T (2015). Investigation of the Focal Spot Drift in Industrial Cone-beam X-ray Computed Tomography. Digit. Ind. Radiol. Comput. Tomogr., June, pp. 22–25

[101] Flay N (2016). An investigation of the factors associated with the X-ray tube and their influence on dimensional measurement in micro-focus cone-beam industrial X-ray computed tomography systems. PhD dissertation, University of Southampton.

[102] Fröhler B, Weissenböck J, Schiwarth M, Kastner J, Heinzl C (2019). open_iA: A tool for processing and visual analysis of industrial computed tomography datasets. Journal of Open Source Software, 4(35), 1185.

[103] Giedl-Wagner R, Miller T, Sick B (2012), Determination of Optimal CT Scan Parameters Using Radial Basis Function Neural Networks. Proc. iCT2012 Conference on Industrial Computed Tomography, Wels, 19-21 September.

[104] Gjsteby L, De Man B, Jin Y, Paganetti H, Verburg J, Giantsoudi D, Wang G (2016) Metal Artifact Reduction in CT: Where Are We After Four Decades? IEEE Access, 4, 5826 – 5849.

[105] Gobert C, Kudzal A, Sietins J, Mock C, Sun J, McWilliams B (2020). Porosity segmentation in X-ray computed tomography scans of metal additively manufactured specimens with machine learning. Addit. Manuf. 36:101460.

[106] Gransfors PR (2003). DQE methodology: step by step. AAPM 45th Annu. Meeting.

[107] Grass M, Kohler T, Proksa R (2000). 3D cone-beam CT reconstruction for circular trajectories. Physics in Medicine and Biology, 45(2):329–347.

[108] Grozmani N, Buratti A, Schmitt RH (2019). Investigating the influence of workpiece placement on the uncertainty of measurements in industrial computed tomography. Proc. iCT2019 Conference on Industrial Computed Tomography, Padova, Italy, 13-15 February.

[109] Gruse JN, Streeter MJV, Thornton C, Armstrong CD, Baird CD, Bourgeois N, Cipiccia S, Finlaye OJ, Gregory CD, Katzir Y, Lopes NC, Mangles SPD, Najmudin Z, Neely D, Pickard LR, Potter KD, Rajeev PP, Rusby DR, Underwood CID, Warnett JM, Williams MA, Wood JC, Murphy CD, Brenner CM, Symes DR (2020). Application of compact laser-driven accelerator X-ray sources for industrial imaging. Nuclear Instruments and Methods in Physics Research Section A: Accelerators, Spectrometers, Detectors and Associated Equipment, 983, 164369.

[110] Hansen DC, Sørensen TS, Rit S (2016). Fast reconstruction of low dose proton CT by sinogram interpolation. Physics in Medicine & Biology, 61(15), 5868.

[111] Hasan MK, Sadi F, Lee SY (2012). Removal of ring artifacts in micro-CT imaging using iterative morphological filters. SIViP , 6: 41-53.

[112] Haugh MJ, Charest MR, Ross PW, Lee JJ, Schneider MB, Palmer NE, Teruya AT (2012). Calibration of X-ray imaging devices for accurate intensity measurement. Powder Diffr 27(2):79–86.

[113] Heinzl C, Kastner J, Amirkhanov A, Gröller E, Gusenbauer C (2012) Optimal specimen placement in cone beam X-ray computed tomography, NDT&E Int. 50:42–49.

[114] Helmecke E, Fleßner M, Gröschl A, Staude A, Hausotte T (2015). Numerical measurement uncertainty determination for computed tomography in dimensional metrology. Proc. XXI MMEKO Congress, Prague.

[115] Herl G, Hiller J, Maier A (2020). Scanning trajectory optimisation using a quantitative Tuybased local quality estimation for robot-based X-ray computed tomography. Nondestructive Testing and Evaluation, 35(3), 287-303.

[116] Herman GT (1979). Correction for beam hardening in computed tomography. Physics in Medicine & Biology, 24(1), 81.

[117] Hermanek P, Carmignato S (2016). Reference object for evaluating the accuracy of porosity measurements by X-ray computed tomography. Case Studies in Nondestructive Testing and Evaluation, 6(B):122-127.

[118] Hermanek P, Carmignato S (2017). Porosity measurements by X-ray computed tomography: Accuracy evaluation using a calibrated object. Precision Engineering, 49, 377-387.

[119] Hermanek P, Zanini F, Carmignato S (2019). Traceable porosity measurements in industrial components using X-ray computed tomography. J. Manuf. Sci. Eng. Trans. ASME. 141:051004.

[120] Hiller J, Kasperl S, Schön T, Schröpfer S, Weiss D (2010). Comparison of probing error in dimensional measurement by means of 3D computed tomography with circular and helical sampling. In 2nd International Symposium on NDT in Aerospace, pp. 1-7.

[121] Hiller J, Reindl LM (2012). A computer simulation platform for the estimation of measurement uncertainties in dimensional X-ray computed tomography. Measurement, 4:2166-2182.

[122] Hiller J, Maisl M, Reindl LM (2012). Physical characterization and performance evaluation of an x-ray micro-computed tomography system for dimensional metrology applications. Measurement Science and Technology, 23(8), 085404.

[123] Hiller J, Genta G, Barbato G, De Chiffre L, Levi R (2014). Measurement uncertainty evaluation in dimensional X-ray computed tomography using the bootstrap method. International Journal of Precision Engineering and Manufacturing,15, 617–622.

[124] Hiller J, Hornberger P (2016). Measurement accuracy in X-ray computed tomography metrology: Toward a systematic analysis of interference effects in tomographic imaging. Precision Engineering, 45, 18-32.

[125] Hiller J, Landstorfer P, Marx P, Herbst M (2020). Evaluation of the impact of faulty scanning trajectories in robot-based x-ray computed tomography. Measurement Science and Technology, 32(1), 015401.

[126] Hornberger B, Kasahara J, Gifford M, Ruth R, Loewen R (2019). A compact light source providing high-flux, quasi-monochromatic, tunable X-rays in the laboratory. Advances in Laboratory-based X-Ray Sources, Optics, and Applications VII, Vol. 11110, p. 1111003. International Society for Optics and Photonics.

[127] Hsieh J, Molthen RC, Dawson CA, Johnson RH (2000). An iterative approach to the beam hardening correction in cone beam CT. Medical physics, 27(1), 23-29.

[128] Hunter AK, McDavid WD (2012). Characterization and correction of cupping effect artefacts in cone beam CT. Dentomaxillofacial Radiology, 41(3), 217-223.

[129] IEC 60336 (2005). Medical Electrical Equipment – X-Ray Tube Assemblies for Medical Diagnosis – Characteristics of Focal Spots.

[130] IEC 62220-1 (2015). Medical electrical equipment - Characteristics of digital X-ray imaging devices - Part 1-1: Determination of the detective quantum efficiency - Detectors used in radiographic imaging.

[131] Illemann J, Bartscher M, Jusko O, Härtig F, Neuschaefer-Rube U, Wendt K (2014) Procedure and reference standard to determine the structural resolution in coordinate metrology. Meas Sci Technol 25:6.

[132] Illemann J, Bartscher M, Neuschaefer-Rube U (2015). An efficient procedure for traceable dimensional measurements and the characterization of industrial CT systems. Proc. Digital Industrial Radiology and Computed Tomography, Ghent.

[133] Illemann J, Bartscher M (2017). X-ray spectrum dependence of the magnification of cone-beam CT spectrum. Proc. iCT2017 Conference on Industrial Computed Tomography, Leuven, 7-9 February.

[134] Illemann J, Neuschaefer-Rube U, Bartscher M, Bate D (2018). Determining spectrum-dependent source and detector positions in cone-beam CT. In Proc. iCT2018 Conf. on Industrial Computed Tomography, Wels.

[135] Illemann J (2020) Traceable measurement of the instrument transfer function in dXCT. Proc. iCT2020 Conference on Industrial Computed Tomography, Wels, 4-7 February.

[136] Illers H, Buhr E and Hoeschen C (2005). Measurement of the detective quantum efficiency (DQE) of digital x-ray detectors according to the novel Standrad IEC 62220-1 Radiat. Prot. Dosim. 114 39–44.

[137] Ingachevaab AS, Buzmakovb AB (2019). Methods of Preprocessing Tomographic Images Taking into Account the Thermal Instability of the X-ray Tube. Optoelectronics, Instrumentation and Data Processing, 55, No. 2, pp. 42–53

[138] Iskender B, Bresler Y (2020). A Physics-Motivated DNN for X-Ray CT Scatter Correction. In 2020 IEEE 17th International Symposium on Biomedical Imaging (ISBI), pp. 609-613. IEEE.

[139] ISO 4287:2000. Geometrical Product Specifications (GPS) — Surface texture: Profile method — Terms, definitions and surface texture parameters.

[140] ISO 10360-5:2010. Geometrical product specifications (GPS) — Acceptance and reverification tests for coordinate measuring machines (CMM) — Part 5: CMMs using single and multiple stylus contacting probing systems

[141] ISO/DIS 10360-11. Geometrical product specifications (GPS) — Acceptance and reverification tests for coordinate measuring systems (CMS) — Part 11: CMSs using the principle of X-ray computed tomography (CT)

[142] ISO 14253-5:2015. Geometrical product specifications (GPS) — Inspection by measurement of workpieces and measuring equipment — Part 5: Uncertainty in verification testing of indicating measuring instruments

[143] ISO 15530-1:2013. Geometrical product specifications (GPS) — Coordinate measuring machines (CMM): Technique for determining the uncertainty of measurement — Part 1: Overview and metrological characteristics, International Organization for Standardization.

[144] ISO 15530-3:2011. Geometrical product specifications (GPS) — Coordinate measuring machines (CMM): Technique for determining the uncertainty of measurement — Part 3: Use of calibrated workpieces or measurement standards

[145] ISO/TS 15530-4:2008. Geometrical product specifications (GPS) - Coordinate measuring machines (CMM): Technique for determining the uncertainty of measurement - Part 4: Evaluating CMM uncertainty using task specific simulation, International Organization for Standardization.

[146] ISO 25178-70:2014. Geometrical product specifications (GPS) — Surface texture: Areal — Part 70: Material measures. International Organization for Standardization.

[147] ISO 25178-600:2019. Geometrical product specifications (GPS) — Surface texture: Areal — Part 600: Metrological characteristics for areal topography measuring methods, International Organization for Standardization.

[148] ISO/IEC GUIDE 99:2007 International vocabulary of metrology — Basic and general concepts and associated terms (VIM).

[149] JCGM 100:2008. Evaluation of measurement data — Guide to the expression of uncertainty in measurement.

[150] Jiménez R, Torralba M, Yagüe-Fabra JA, Ontiveros S, Tosello G (2017). Experimental approach for the uncertainty assessment of 3D complex geometry dimensional measurements using computed tomography at the mm and sub-mm scales. Sensors 17:1137.

[151] Joseph PM, Spital, RD (1978). A method for correcting bone induced artifacts in computed tomography scanners. Journal of computer assisted tomography, 2(1), 100-108.

[152] Joseph PM, Schulz RA (1980). View sampling requirements in fan beam computed tomography, Medical physics, 7(6), 692-702.

[153] Kachelrieß M, Sourbelle K, Kalender WA (2006). Empirical cupping correction: A first-order raw data precorrection for cone-beam computed tomography. Medical physics, 33(5), 1269-1274.

[154] Kalender WA (2011). Computed tomography: fundamentals, system technology, image quality, applications. John Wiley & Sons.

[155] Kang R, Probst GM, Slaets P, Dewulf W (2020). Investigation of the impact of various robot properties on a twin Robot-CT system. Nondestructive Testing and Evaluation, 35(3), 276-286.

[156] Katić M, Baršić G (2019). Comparison of different voxel size calibration strategies. iCT2019 Conference on Industrial Computed Tomography, Padova, 13-15 February.

[157] Kerckhofs G (2009). Morphological and mechanical quantification of porous structures by means of micro-CT. PhD Dissertation, KU Leuven.

[158] Kiekens K, Welkenhuyzen F, Tan Y, Bleys P, Voet A, Kruth JP, Dewulf W (2011). A test object with parallel grooves for calibration and accuracy assessment of industrial computed tomography (CT) metrology. Measurement Science and Technology, 22(11), 115502.

[159] Konopczyński T, Rathore D, Rathore J, Kröger T, Zheng L, Garbe CS, Carmignato S & Hesser J (2019). Fully convolutional deep network architectures for automatic short glass fiber semantic segmentation from ct scans. arXiv preprint arXiv:1901.01211.

[160] Konstantinidis A (2011). Evaluation of digital X-ray detectors for medical imaging applications. PhD thesis. University College London.

[161] Körner L, Lawes S, Bate D, Newton L, Senin N, Leach RK (2019). Increasing throughput in x-ray computed tomography measurement of surface topography using sinogram interpolation. Measurement Science and Technology, 30(12), 125002.

[162] Kraemer A, Lanza G (2016) Assessment of the measurement procedure for dimensional metrology with X-ray computed tomography. Procedia CIRP 43:362–367

[163] Kratz, B., Herold, F., Robbins, J. C., & Tamm, J. Study on the Influence of Scattered Radiation and the Usage of Scatter Reduction Methods for Computed Tomography. Proc. iCT 2017 Conference on Industrial Computed Tomography, Leuven, 7-9 February.

[164] Kritikos M (2021). Porosity measurement by X-ray computed tomography: different porosity analysis application. In: Lecture Notes in Mechanical Engineering, 175–185, Springer, Berlin.

[165] Krumm M, Kasperl S, Franz M (2008), Reducing non-linear artifacts of multi-material objects in industrial 3D computed tomography. NDT & E International, 41, 242-251, Doi: 10.1016/j.ndteint.2007.12.001.

[166] Kruth JP, Bartscher M, Carmignato S, Schmitt R, De Chiffre L, Weckenmann A (2011). Computed tomography for dimensional metrology. CIRP Annals - Manufacturing Technology, 60, 821–842.

[167] Kumar J, Attridge A, Wood PKC, Williams MA (2011). Analysis of the effect of cone-beam geometry and test object configuration on the measurement accuracy of a computed tomography scanner used for dimensional measurement Meas. Sci. Technol. 22 035105.

[168] Kuusk J (2011) Dark signal temperature dependence correction method for miniature spectrometer modules. J Sens 2011:1-9, doi:10.1155/2011/608157.

[169] Kwan ALC, Seibert JA, Boone JM (2006). An improved method for flat-field correction of flat panel x-ray detector. Med Phys 33(2):391–393.

[170] Kyrieleis A, Ibison M, Titarenko V, Withers PJ (2009). Image stitching strategies for tomographic imaging of large objects at high resolution at synchrotron sources. Nucl. Instr. Meth. Phys. Res. A 607, 677–684.

[171] Kyrieleis A, Titarenko V, Ibison M, Connolley T, Withers PJ (2011). Region-of-interest tomography using filtered backprojection: assessing the practical limits. J Microsc. 241(1):69-82.

[172] Landstorfer P, Hiller J, Herbst M (2019). Investigation of positioning accuracy of industrial robots for robotic-based X-Ray computed tomography. Proc. iCT2019 conference of industrial computed tomography, Padova, 13-15 February, pp. 13-15.

[173] Larsson DH, Vågberg W, Yaroshenko A, Yildirim AÖ, Hertz HM (2016). High-resolution short-exposure small-animal laboratory X-ray phase-contrast tomography. Sci. Rep. 6, 39074.

[174] Leach RK, Bourell D, Carmignato S, Donmez A, Senin N, Dewulf W (2019). Geometrical metrology for metal additive manufacturing. CIRP annals, 68(2), 677-700.

[175] Leach RK, Haitjema H, Su R, Thompson A (2020). Metrological characteristics for the calibration of surface topography measuring instruments: a review. Meas. Sci. Technol. 32:032001.

[176] Leach RK (2020). Advances in Optical Form and Coordinate Metrology, IOP Publishing.

[177] Léonard F, Brown SB, Withers PJ, Mummery PM, McCarthy MB (2014). A new method of performance verification for x-ray computed tomography measurements. Measurement Science and Technology, 25(6), 065401.

[178] Lettenbauer H, Georgi B, Weiß D (2007). Means to verify the accuracy of CT systems for metrology applications (in the absence of established international standards). Proc. Int. Symp. Digital Industrial Radiology and Computed Tomography, Lyon.

[179] Li H, Mohan R, Zhu XR (2008). Scatter kernel estimation with an edge-spread function method for cone-beam computed tomography imaging. Physics in Medicine & Biology, 53(23), 6729.

[180] Liang X, Li N, Zhang Z, Yu S, Qin W, Li Y, Chen Q, Zhang H, Xie Y (2019). Shading correction for volumetric CT using deep convolutional neural network and adaptive filter. Quantitative imaging in medicine and surgery, 9(7), 1242.

[181] Lifton JJ (2015) The Influence of Scatter and Beam Hardening in X-ray Computed Tomography for Dimensional Metrology. PhD Thesis, University of Southampton.

[182] Lifton, JJ, Malcolm AA, McBride JW (2015). On the uncertainty of surface determination in x-ray computed tomography for dimensional metrology. Meas. Sci. Technol. 26:035003.

[183] Lifton JJ, Malcolm AA, McBride JW (2015). A simulation-based study on the influence of beam hardening in X-ray computed tomography for dimensional metrology. Journal of X-ray Science and Technology, 23(1), 65-82.

[184] Lifton JJ, Carmignato S. (2017). Simulating the influence of scatter and beam hardening in dimensional computed tomography. Measurement Science and Technology, 28(10), 104001.

[185] Lifton JJ, Liu T (2020). Evaluation of the standard measurement uncertainty due to the ISO50 surface determination method for dimensional computed tomography. Precision Engineering, 61, 82-92.

[186] Lifton J, Liu T (2021). An adaptive thresholding algorithm for porosity measurement of additively manufactured metal test samples via X-ray computed tomography. Addit. Manuf. 39:101899.

[187] Lüthi M, Bircher BA, Meli F, Küng A, Thalmann R (2019). X-ray flat-panel detector geometry correction to improve dimensional computed tomography measurements. Meas. Sci. Technol. 31.

[188] Maier J, Sawall S, Knaup M, Kachelrieß M (2018). Deep scatter estimation (DSE): accurate real-time scatter estimation for X-ray CT using a deep convolutional neural network. Journal of Nondestructive Evaluation, 37(3), 1-9.

[189] Marinello F, Savio E, Carmignato S, De Chiffre L. (2008). Calibration artefact for the microscale with high aspect ratio: The fiber gauge. CIRP annals, 57(1), 497-500.

[190] Martz HE, Logan CM, Schneberk DJ, Shull PJ (2016). X-ray Imaging: fundamentals, industrial techniques and applications. CRC Press.

[191] McDavid WD, Waggener RG, Payne WH, Dennis MJ (1977). Correction for spectral artifacts in cross-sectional reconstruction from x rays. Medical physics, 4(1), 54-57.

[192] Miceli A, Thierry R, Flisch A, Sennhauser U, Casali F, Simon M (2007) Monte Carlo simulations of a high-resolution X-ray CT system for industrial applications. Nuclear Instruments and Methods in Physics Research A 583, 313-323.

[193] Mohaghegh K, Andreasen JL, De Chiffre L (2020). Investigation on the effect of filtering and plane fitting strategies on differences between XCT and CMM measurements on a miniature step gauge. Proc. iCT2020 Conference on Industrial Computed Tomography, Wels, 4-7 February.

[194] Muralikrishnan B, Shilling M, Phillips S, Ren W, Lee V, Kim F (2019). X-ray computed tomography instrument performance evaluation, Part I: Sensitivity to detector geometry errors. Journal of Research of the National Institute of Standards and Technology, 124, 1-16.

[195] Muralikrishnan B, Shilling M, Phillips S, Ren W, Lee V and Kim F (2019). X-ray computed tomography instrument performance evaluation, Part II: Sensitivity of rotation stage errors. J. Res. NIST 124:1-13.

[196] Müller AM, Hausotte T (2019). Comparison of different measures for the single point uncertainty in industrial X-ray computed tomography. In iCT2019 Conference on Industrial Computed Tomography, Padova, 13-15 February.

[197] Müller AM, Butzhammer L, Wohlgemuth F, Hausotte T (2020). Automated evaluation of the surface point quality in dimensional X-ray computed tomography. tm-Technisches Messen, 87(2), 111-121.

[198] Müller P, Hiller J, Cantatore A, De Chiffre L (2012) A study on evaluation strategies in dimensional X-ray computed tomography by estimation of measurement uncertainties. Int J Metrol Qual Eng 3:107–115.

[199] Müller P (2013). Coordinate metrology by traceable computed tomography, PhD Thesis. Technical University of Denmark.

[200] Müller P, Cantatore A, Andreasen JL, Hiller J, De Chiffre L (2013) Computed tomography as a tool for tolerance verification of industrial parts. Procedia CIRP 10:125–132.

[201] Müller P, Hiller J, Dai Y, Andreasen JL, Hansen HN, De Chiffre L (2014). Estimation of measurement uncertainties in X-ray computed tomography metrology using the substitution method. CIRP Journal of Manufacturing Science and Technology, 7(3), 222-232.

[202] Münch B, Trtik P, Marone F, Stampanoni M (2009). Stripe and ring artifact removal with combined wavelet-Fourier filtering. Opt Express 17(10):8567-8591.

[203] Nardelli VC, Donatelli GD, Arenhart FA, Porath MC (2011). Uncertainty evaluation of computed tomography measurements using multiple calibrated workpieces. II CIMMEC, Natal, Brazil.

[204] Obaton AF, Klingaa CG, Rivet C, Mohaghegh K, Baier S, Andreasen JL, Carli L, De Chiffre L (2020) Reference standards for XCT measurements of additively manufactured parts, iCT2020 Conference on Industrial Computed Tomography, Wels, 4-7 February.

[205] Obaton AF, Yardin C, Liltorp K, Quagliotti D, De Chiffre L (2022) Comparison campaign of XCT systems using machined standards representative of additively manufactured parts. Proc. iCT2022 Conference on Industrial Computed Tomography, Wels, 8-11 February.

[206] Orhan K, de Faria Vasconcelos K, Gaêta-Araujo H (2020) Artifacts in Micro-CT. In: Orhan K Micro-computed Tomography (micro-CT) in Medicine and Engineering, 35-48, Springer, Cham. Doi: 10.1007/978-3-030-16641-0_4.

[207] Ortega N, Plaza S, Pascual A, Holgado I, Lamikiz A (2021). A methodology to obtain traceability for internal and external measurements of Inconel 718 components by means of XRCT. NDT & E International 120:102436.

[208] Otsu N (1979). A threshold selection method from gray-level histograms, IEEE Transactions on Systems, Man, and Cybernetics, vol. 9, no. 1, pp. 62-66.

[209] Pagani L, Townsend A, Zeng W, Lou S, Blunt L, Jiang XQ, Scott PJ (2019). Towards a new definition of areal surface texture parameters on freeform surface: Re-entrant features and functional parameters. Measurement, 141, 442-459.

[210] Panas R, Cuadra JA, Mohan KA, Morales RE (2021). A Systems Approach to Estimating the Uncertainty Limits of X-Ray Radiographic Metrology. Journal of Micro- and Nano-Manufacturing 9, 010901.

[211] Pavan M, Craeghs T, Kruth JP, Dewulf W (2018). Investigating the influence of X-ray CT parameters on porosity measurement of laser sintered PA12 parts using a design-of-experiment approach. Polymer Testing, 66, 203-212.

[212] Pelt DM, Batenburg KJ, Sethian JA (2018). Improving Tomographic Reconstruction from Limited Data Using Mixed-Scale Dense Convolutional Neural Networks. J. Imaging 2018, 4, 128.

[213] Poludniovski G, Evans P, DeBlois F, Landry G, Verhaegen F. SpekCalc 2009. http://spekcalc.weebly.com/

[214] Prell D, Kyriakou Y, Kalender WA (2009). Comparison of ring artifact correction methods for flat-detector CT. Phys Med Biol 54:3881-3895.

[215] Probst G, Pavan M, Rathore J, Craeghs T, Kruth JP, Carmignato S, Dewulf W (2015). Influence of Electron Beam Alignment on Dimensional Metrology by Computed Tomography. In Proceedings of the 2015 International Symposium on Digital Industrial Radiology and Computed Tomography.

[216] Probst G, Kruth JP, Dewulf W (2016). Compensation of drift in an industrial computed tomography system. Proc. iCT2016 conference on industrial computed tomography, Wels, 9-12 February.

[217] Probst GM, Hou Q, Boeckmans B, Xiao Y, Dewulf W (2020). Characterization and stability monitoring of X-ray focal spots. CIRP Annals, 69(1), 453-456.

[218] Probst GM (2022). Methods for assessing source and manipulator stability in Dimensional X-ray Computed Tomography. KU Leuven.

[219] Pyka G, Kerckhofs G, Braem A, Mattheys T, Schrooten J, Wevers M (2010). Novel micro-ct based characterization tool for surface roughness measurements of porous structures. In: SkyScan User Meeting (pp. 1-5).

[220] Rangayyan R, Dhawan AP, Gordon R (1985). Algorithms for limited-view computed tomography: an annotated bibliography and a challenge. Applied optics, 24(23), 4000-4012.

[221] Reiter M, de Oliveira FB, Bartscher M, Gusenbauer C, Kastner J (2019). Case study of empirical beam hardening correction methods for dimensional x-ray computed tomography using a dedicated multi-material reference standard. Journal of Nondestructive Evaluation, 38(1), 1-15.

[222] Rieth-Hoerst S, Reinhart C, Günther T, Dierig T, Fieres J (2014). Methods to ensure accuracy and reliability of analyses and measurements done on CT data-sets. In: Proceedings of 11th European Conference on Non-Destructive Testing, Prague, 6-11 October.

[223] Rodriguez-Sánchez Á, Thompson A, Körner L, Brierley N, Leach RK (2020). Review of the influence of noise in X-ray computed tomography measurement uncertainty. Precision Engineering, Vol. 66, pp. 382-391.

[224] Rodríguez-Sánchez A, Thompson A, Senin N, Eifler M, Hering J, Leach RK (2021). Calibration of X-ray computed tomography for surface texture measurement using metrological characteristics. Proc. 21st Int. euspen Conf.

[225] Rothleitner C, Neuschaefer-Rube U, Illemann J (2016). Size and shape determination of sub-millimeter sized abrasive particles with X-ray computed tomography. In Proc. iCT2016 Conference on Industrial Computed Tomography, Wels, 9-12 February.

[226] Rüegsegger P, Hangartner T, Keller HU, Hinderling T (1978). Standardization of computed tomography images by means of a material-selective beam hardening correction. Journal of Computer Assisted Tomography, 2(2), 184-188.

[227] Salesbury JG (2012) Developments in the international standardization of testing methods for CMMs with imaging probing systems. NCSL International Workshop & Symposium.

[228] Santos VMR, Thompson A, Sims-Waterhouse D, Maskery I, Woolliams P, Leach RK (2020). Design and characterisation of an additive manufacturing benchmarking artefact following a design-for-metrology approach. Additive Manufacturing, 32, 100964.

[229] Sbettega E, Zanini F, Carmignato S (2021). Sensitivity analysis of the geometrical misalignments of X-ray computed tomography systems on dimensional measurements. Proc. Euspen 21st International Conference & Exhibition, 7-10 June.

[230] Schild L, Häfner B, Lanza G (2018). Knowledge Based User Support for Computed Tomography Measurements. In Congress of the German Academic Association for Production Technology (pp. 667-678). Springer.

[231] Schild L, Jung M, Häfner B, Lanza G (2020). Influence of different mounting strategies on the random measurement error in industrial computed tomography. Proc. iCT2020 Conference on Industrial Computed Tomography, Wels, 4-7 February.

[232] Schmidgunst C, Ritter D, Lang E (2007). Calibration model of a dual gain flat panel detector for 2D and 3D X-ray imaging. Med Phys 34(9):3649–3664.

[233] Schmitt R, Niggemann C (2010). Uncertainty in measurement for x-ray-computed tomography using calibrated work pieces. Measurement Science and Technology, 21(5), 054008.

[234] Schmitt R, Isenberg C, Niggemann C (2012) Knowledge-based system to improve dimensional CT measurements. Proc. iCT2012 Conference on industrial computed tomography, Wels, 19-21 September.

[235] Schorner K, Goldammer M, Stierstorfer K, Stephan J, Boni P (2012). Scatter correction method by temporal primary modulation in x-ray CT. IEEE Transactions on Nuclear Science, 59(6), 3278-3285.

[236] Schörner K (2012) Development of Methods for Scatter Artifact Correction in Industrial X-ray Cone-beam Computed Tomography. PhD Thesis, Technische Universität München.

[237] Schuetz P, Jerjen I, Hofmann J, Plamondon M, Flisch A, Sennhauser U (2014) Correction algorithm for environmental scattering in industrial computed tomography. NDT E Int Volume 64:59–64.

[238] Seeram E (2015). Computed tomography: physical principles, clinical applications, and quality control. Elsevier Health Sciences.

[239] Sezgin M, Sankur B (2004). Survey over image thresholding techniques and quantitative performance evaluation. J. Electron Imaging 13(1):146-168.

[240] Senin N, Catalucci S, Moretti M, Leach RK (2021). Statistical point cloud model to investigate measurement uncertainty in coordinate metrology. Prec. Eng. 70:44-62.

[241] Shi L, Bennett NR, Wang AS (2021). Characterization of x-ray focal spots using a rotating edge. Journal of Medical Imaging, 8(2), 023502.

[242] Shu S, Dai N, Cheng X, Zhou X, Wang L, Villarraga-Gómez H (2019). A study on factors influencing the accuracy evaluatiom of dimensional X-ray computed tomography with multi-sphere standards, Int. J. Prec. Eng. Manufac. 7.

[243] Sidky EY, Yu L, Pan X, Zou Y, Vannier M (2005). A robust method of X-ray source spectrum estimation from transmission measurements: Demonstrated on computer simulated, scatter-free transmission data. Journal of applied physics 97/12, 124701.

[244] Sidky EY, Kao CM, Pan X (2006). Accurate image reconstruction from few-views and limited-angle data in divergent-beam CT. Journal of X-ray Science and Technology, 14(2), 119-139.

[245] Sijbers J, Postnov A (2004). Reduction of Ring Artifacts in High Resolution Micro-CT Reconstructions. Phys Med Biol 49(14):247-253.

[246] Sinico M, Ametova E, Witvrouw A, Dewulf W (2018). Characterization of AM metal powder with an industrial microfocus CT: Potential and limitations. In Proceedings of 2018 Summer Topical Meeting on Advancing Precision in Additive Manufacturing (Vol. 69, pp. 286-291). American Society for Precision Engineering.

[247] Sinico M, Dewulf W, Witvrouw A (2019). The role of powder properties on precision additive metal manufacturing. In Additive Manufacturing Workshop 2019-Present and future of Additive Manufacturing in Industry and Research, Date: 2019/09/20-2019/09/20, Location: Padova (PD), IT.

[248] Sittner J, Godinho JRA, Renno AD, Cnudde V, Boone M, De Schryver T, Van Loo D, Merkulova M, Roine A, Liipo J (2020). Spectral X-ray computed micro tomography: 3-dimensional chemical imaging. X- Ray Spectrometry, 50(2), pp.92-105.

[249] Six N, De Beenhouwer J, Sijbers J (2019). Poly-DART: A discrete algebraic reconstruction technique for polychromatic X-ray CT. Optics Express 27 (23), 33670-33682.

[250] Skaarup M, Edmund J, Kachelriess M, Vogelius I (2020). PO-1739: A deep learning neural network to remove metal artefacts via residual learning for cone-beam CT. Radiotherapy and Oncology, 152, S964-S965.

[251] Stenner P, Berkus T, Kachelriess M (2007). Empirical dual energy calibration (EDEC) for cone-beam computed tomography. Medical physics, 34(9), 3630-3641.

[252] Stock SR (2019). MicroComputed Tomography: Methodology and Applications, 2nd edn, Taylor & Francis.

[253] Stolfi A, Thompson MK, Carli L, De Chiffre L (2016). Quantifying the contribution of post-processing in computed tomography measurement uncertainty. Procedia CIRP, 43, 297-302.

[254] Stolfi A, De Chiffre L (2016). 3D artefact for concurrent scale calibration in Computed Tomography CIRP Annals, 65:1, 499–502.

[255] Stolfi A (2017). Integrated quality control of precision assemblies using computed tomography. PhD Dissertation. Technical University of Denmark.

[256] Stolfi A, De Chiffre L, Kasperl S (2018). Error Sources. In: Carmignato S, Dewulf W, Leach R. Industrial X-ray Computed Tomography. Springer.

[257] Stolfi A, De Chiffre L, 2018, Interlaboratory comparison of a physical and a virtual assembly measured by CT. Prec. Eng. 51:263-270.

[258] Sun M, Star-Lack JM (2010). Improved scatter correction using adaptive scatter kernel superposition. Physics in Medicine & Biology, 55(22), 6695.

[259] Synek V (2005). Attempts to include uncorrected bias in the measurement uncertainty. Talanta 65:829-837.

[260] Szeles C (2014). CdZnTe and CdTe materials for X-ray and gamma ray radiation detector applications. physica status solidi (b) 241/3, 783–790.

[261] Tang X, Ning R, Yu R, Conover D (2001). Cone beam volume CT image artifacts caused by defective cells in x-ray flat panel imagers and the artifact removal using a wavelet-analysis-based algorithm. Med Phys 28(5):812-825.

[262] Tate MW, Chamberlain D, Gruner SM (2005). Area X-ray detector based on a lens-coupled charge-coupled device. Rev Sci Instrum 76:081301.

[263] Thierry R, Miceli A, Hofmann J (2007). Hybrid simulation of scattering distribution in cone beam CT. Proc. International symposium on digital industrial radiology and computed tomography, pp. 25-27.

[264] Thompson A, Senin N, Giusca C, Leach RK (2017). Topography of selectively laser melted surfaces: A comparison of different measurement methods. Ann. CIRP 66:543–546.

[265] Thompson A, Senin N, Maskery I, Körner L, Lawes S, Leach RK (2018). Internal surface measurement of metal powder bed fusion parts. Addit. Manuf. 20:126–133.

[266] Thompson A, Senin N, Maskery I, Leach RK (2018). Effects of magnification and sampling resolution in X-ray computed tomography for the measurement of additively manufactured metal surfaces. Precision Engineering, 53, 54-64.

[267] Torralba M, Jiménez R, Yagüe-Fabra JA, Ontiveros S, Tosello G (2018) Comparison of surface extraction techniques performance in computed tomography for 3D complex micro-geometry dimensional measurements. International Journal of Advanced Manufacturing Technology, 97, 441–453.

[268] Townsend A, Pagani L, Blunt L, Scott PJ, Jiang X (2017). Factors affecting the accuracy of areal surface texture data extraction from X-ray CT. CIRP Annals, 66(1), 547-550.

[269] Turner N, Brierley N, Townsend A (2019) 3-in-1 X-ray computed tomography. Proc. iCT2019 Conference on Industrial Computed Tomography, Padova, 13-15 February.

[270] Tuy HK (1983). An inversion formula for cone-beam reconstruction. SIAM Journal on Applied Mathematics, 43(3), 546-552.

[271] Van Laere K, Koole M, Lemahieu I, Dierckx R. (2001) Image filtering in single-photon emission computed tomography: principles and applications Comput. Med Imag Grap 2001;25:127–33.

[272] VDI/VDE 2630 Blatt 1.3 (2011) Computed tomography in dimensional measurement - Guideline for the application of DIN EN ISO 10360 for coordinate measuring machines with CT-sensors.

[273] VDI/VDE 2630 Blatt 2.1 (2015) Computed tomography in dimensional measurement - Determination of the uncertainty of measurement and the test process suitability of coordinate measurement systems with CT sensors.

[274] Villarraga-Gómez H, Lee C, Smith ST (2018). Dimensional metrology with X-ray CT: A comparison with CMM measurements on internal features and compliant structures. Prec. Eng. 51:291-307.

[275] Villarraga-Gómez H (2018) Studies of dimensional metrology with X-ray CAT scan. PhD dissertation, The University of North Carolina at Charlotte.

[276] Villarraga-Gómez H, Herazo EL, Smith ST (2019). X-ray computed tomography: from medical imaging to dimensional metrology. Precision Engineering, 60, 544-569.

[277] Villarraga-Gómez H, Smith ST (2020). Effect of the number of projections on dimensional measurements with X-ray computed tomography. Precision Engineering, 66, 445-456.

[278] Villarraga-Gómez H, Thousand JD, Smith ST (2020). Empirical approaches to uncertainty analysis of X-ray computed tomography measurements: A review with examples. Prec. Eng. 64:249-268.

[279] Villarraga-Gómez H, Amirkhanov A, Heinzl C, Smith ST (2021). Assessing the effect of sample orientation on dimensional X-ray computed tomography through experimental and simulated data. Measurement, 178, 109343.

[280] Visual Computing Lab - ISTI - CNR 2018 MeshLab (Available at https://www.meshlab.net/) Accessed: 14th June 2021.

[281] Vlaeyen M, Haitjema H, Dewulf W (2021). Digital Twin of an Optical Measurement System. Sensors, 21(19), 6638.

[282] Vo NT, Atwood RC, Drakopoulos M (2018). Superior techniques for eliminating ring artifacts in X-ray micro-tomography. Optics express, 26(22), 28396-28412.

[283] Vogeler F, Verheecke W, Voet A, Kruth JP, Dewulf W (2011). Positional stability of 2D x-ray images for computer tomography. Proc. Int. Symp. on Digital Industrial Radiology and Computed Tomography, Berlin.

[284] VolumeGraphics 2021 VGStudioMAX 3.5 (Available at https://www.volumegraphics.com/) Accessed: 14th June 2021.

[285] Wang B, Chen Z, Dewulf W, Pauwels R, Yao Z, Hou Q, Xiao Y. (2019). U-net-based blocked artifacts removal method for dynamic computed tomography. Applied optics, 58(14), 3748-3753.

[286] Wang J, Pagani L, Zhou L, Liu X, Lu W, Leach R K, Jiang X (2019) Uncertainty-guided intelligent sampling strategy for high-efficiency surface measurement via free-knot B-spline regression modelling Prec. Eng. 56 38-52.

[287] Weckenmann A, Krämer P (2013). Computed tomography in quality control: chances and challenges. Proceedings of the Institution of Mechanical Engineers, Part B: Journal of Engineering Manufacture, 227(5), 634-642.

[288] Weiss D, Lonardoni R, Deffner A and Kuhn C (2012). Geometric image distortion in flat-panel x-ray detectors and its influence on the accuracy of CT-based dimensional measurements Proc. iCT2012 Conf. on Industrial Computed Tomography, pp 173–81.

[289] Weissenböck J, Amirkhanov A, Li W, Reh A, Amirkhanov A, Gröller E, Kastner J, Heinzl C (2014). Fiberscout: An interactive tool for exploring and analyzing fiber reinforced polymers. Proc. 2014 IEEE Pacific Visualization Symposium; pp. 153-160, IEEE.

[290] Wen Z, Fahrig R, Conolly S, Pelc NJ (2007). Investigation of electron trajectories of an x-ray tube in magnetic fields of MR scanners. Medical physics, 34(6:1), 2048-2058.

[291] Wenig P, Kasperl S (2006). Examination of the measurement uncertainty on dimensional measurements by X-ray computed tomography. Proc. 9th European Conference on Non-Destructive Testing (ECNDT), Berlin, 19-21 September.

[292] Williams TC, Shaddix CR (2007). Simultaneous correction of flat field and nonlinearity response of intensified charge-coupled devices. Rev Sci Instrum 78:123702.

[293] Withers PJ, Bouman C, Carmignato S, Cnudde V, Grimaldi D, Hagen CK, Maire E, Manley M, Du Plessis A, Stock SR (2021). X-ray computed tomography. Nature Reviews Methods Primers, 1(1), 1-21.

[294] Wits WW, Carmignato S, Zanini F, Vaneker THJ (2016). Porosity testing methods for the quality assessment of selective laser melted parts. CIRP Annals, 65 (1):201–204.

[295] Wohlgemuth F, Müller AM, Hausotte T (2018). Development of a virtual metrological CT for numerical measurement uncertainty determination using aRTist 2, Tech. Mess. 85:728–737.

[296] Wohlgemuth F, Hausotte T (2020). Convergence behaviour of numerical measurement uncertainty evaluation using a virtual metrological computed tomography system, Proc. iCT2020 Conf. Industrial Computed Tomography, Wels.

[297] Würfl T, Ghesu FC, Christlein V, Maier A (2016). Deep learning computed tomography. Proc. MICCAI2016 International conference on medical image computing and computer-assisted intervention, Athens, 17-21 October, pp. 432-440. Springer.

[298] Würfl T, Hoffmann M, Christlein V, Breininger K, Huang Y, Unberath M, Maier AK (2018). Deep Learning Computed Tomography: Learning Projection-Domain Weights From Image Domain in Limited Angle Problems. IEEE Transactions on Medical Imaging, vol. 37, no. 6, pp. 1454-1463.

[299] Xiao X, De Carlo F, Stock S (2007). Practical error estimation in zoom-in and truncated tomography reconstructions. Rev. Sci. Instr. 78, 063705.

[300] Xu Z, Hyde CJ, Thompson A, Leach RK, Maskery I, Tuck C, Clare AT (2017). Staged thermomechanical testing of nickel superalloys produced by selective laser melting. Mater. Des. 133:520–527.

[301] Xue L, Suzuki H, Ohtake Y, Fujimoto H, Abe M, Sato O, Takatsuji T (2015). Numerical analysis of the Feldkamp-Davis-Kress effect on industrial X-ray computed tomography for dimensional metrology, J. Comput. Inf. Sci. Eng. 15 (2).

[302] Yagüe-Fabra JA, Ontiveros S, Jiménez R, Chitchian S, Tosello G, Carmignato S (2013). A 3D edge detection technique for surface extraction in computed tomography for dimensional metrology applications. CIRP Annals, 62(1), 531-534.

[303] Yan H, Mou X, Tang S, Xu Q, Zankl M (2010). Projection correlation based view interpolation for cone beam CT: primary fluence restoration in scatter measurement with a moving beam stop array. Physics in Medicine & Biology, 55(21), 6353.

[304] Yu Y, Wang J (2012). Beam hardening-respecting flat field correction of digital X-ray detectors. IEEE International Conference on Image Processing, 30 September – 3 October, pp 2085–2088.

[305] Yun W, Lau SH, Stripe B, Lyon A, Reynolds D, Lewis SJ, Chen S, Semenov V, Spink RI (2016). Novel, high brightness x-ray source and high efficiency x-ray optic for development of x-ray instrumentation. Microscopy and Microanalysis, 22(S3), 118-119.

[306] Zanini F, Carmignato S (2017) Two-spheres Method for Evaluating the Metrological Structural Resolution in Dimensional Computed Tomography. Measurement Science and Technology 28(11):114002.

[307] Zanini F, Pagani L, Savio E, Carmignato S (2019). Characterisation of additively manufactured metal surfaces by means of X-ray computed tomography and generalised surface texture parameters. Ann. CIRP 68:515–518.

[308] Zanini F, Sbettega E, Sorgato M, Carmignato S (2019). New approach for verifying the accuracy of X-ray computed tomography measurements of surface topographies in additively manufactured metal parts. J. Nondestruc. Eval. 38:12.

[309] Zanini F, Carmignato S (2019). Accuracy of fiber length measurements using X-ray computed tomography for the analysis of composite materials. Proc. Euspen.

[310] Zanini F, Sorgato M, Savio E, Carmignato S (2021). Dimensional verification of metal additively manufactured lattice structures by X-ray computed tomography: Use of a newly developed calibrated artefact to achieve metrological traceability. Additive Manufacturing, 2021, 47, 102229.

[311] Zanini F, Carmignato S, Savio E (2021). Two different experimental approaches for the uncertainty determination of X-ray computed tomography dimensional measurements on complex additively manufactured parts. Precision Engineering, submitted, under revision.

[312] Zemek M, Blažek P, Šrámek J, Šalplachta J, Zikmund T, Klapetek P, Takeda Y, Omote K, Kaiser J (2020) Voxel Size Calibration for High-resolution CT. Proc. iCT2020 Conference on Industrial Computed Tomography, Wels, 4-7 February.

[313] Zhao Z, Gang GJ, Siewerdsen JH (2014). Noise, sampling, and the number of projections in cone-beam CT with a flat-panel detector Med. Phys 2014;41:061909.

[314] Zhu L, Strobel N, Fahrig R (2005). X-ray scatter correction for cone-beam CT using moving blocker array. In Medical Imaging 2005: Physics of Medical Imaging, Vol. 5745, pp. 251-258. International Society for Optics and Photonics.

[315] Zhu Y, Wu Z, Hartley WD, Sietins JM, Williams CB, Hang ZY (2020). Unraveling pore evolution in post-processing of binder jetting materials: X-ray computed tomography, computer vision, and machine learning. Addit. Manuf. 34:101183.

[316] Ziegler A, Kohler T, Proksa R (2007). Noise and resolution in images reconstructed with FBP and OSC algorithms for CT. Med Phys 2007;34:585–98.